Analysis of neutron-rich isotopes around the Z∼38 region populated through a heavy-ion fission reaction

Cesar Yesid Lizarazo Sabogal

Universidad Nacional de Colombia
Facultad de Ciencias, Departamento de Física
Bogotá D.C, Colombia
2013

Analysis of neutron-rich isotopes around the Z∼38 region populated through a heavy-ion fission reaction

Cesar Yesid Lizarazo Sabogal

Tesis submitted in partial fullfillment of the requirements for the Degree of:

Magister in Science - Physics

Director:
Dr. Fernando Cristancho
Universidad Nacional de Colombia.
Bogotá D.C., Colombia

Co-Director:
Dr. Edana Merchán Rodríguez.
University of Massachusetts Lowell.
Lowell MA, U.S.A.

2014

Agradecimientos

A mi Padre, quien me dio la cabeza,
A mi Madre, quien me dio el corazón.

Al Profe, por guiarme con paciencia y confianza en mis errores y aciertos; por lograr con un tinto en mano mientras conversa, lo que pocos consiguen con marcador y tiza: formar profesionales que sean personas a la vez.

A Edana, por la gran cantidad conocimiento y oportunidades que me ha brindado generosamente. Mi sincera admiración por su fortaleza mental para el trabajo y la vida.

A Wilmar, por lo que aprendimos juntos como amigos y colegas, por nuestra retroalimentación que tanto valoro, y que me ha hecho más perseverante en la vida.
Por supuesto al GFNUN, por el excelente ambiente dispuesto para aprender e investigar.

A Mana, Amiga, Paris, y Equipo, por el apoyo leal en todos los momentos gratos y amargos de estos dos años, de una u otra forma ustedes me hacen fuerte en la vida que a diario se goza y se pelea.

A David Paris, Eliana González y Eluned Smith, por su desinteresada -muchas veces sacrificada- ayuda para corregir mi inglés, espero les guste el resultado final.

A la Universidad Nacional, cuya quijotesca misión en este país de amores y dolores es ser mayor a la de formar profesionales, es formar seres humanos de esos que quieren, luchan y construyen una realidad distinta.

Al Centro Internacional de Física - CIF, por financiar los gastos del viaje para la participación del experimento analizado en esta tesis.

A la Vicerrectoría Academica, por la Beca Estudiante Sobresaliente de Posgrado, uno de los mejores estímulos académicos ofrecidos en el país para realizar estudios de Posgrado.

Muchas gracias.

Resumen

El estudio de núcleos ricos en neutrones es uno de los actuales campos de investigación más activos en física nuclear. El exceso de neutrones que estos presentan en comparación con los núcleos estables genera fenómenos físicos no observados previamente, por ejemplos, el cambio en los llamados números mágicos predichos por el modelo de capas nuclear, lo que lleva a comportamientos inesperados de la deformación nuclear para estos isótopos lejos de la línea de estabilidad.

En las ultimas décadas, los isótopos ricos en neutrones con un número de protones (Z) cercano a 38 han ganado atención debido a la evolución de su deformación como función del número de neutrones. El caso más importante corresponde al Zirconio (Z=40), donde la deformación nuclear cambia desde una forma cuasi-esférica para el ^{96}Zr hasta una deformación altamente prolata para el ^{104}Zr. No obstante, el análisis experimental de este fenómeno no se ha completado pues la producción de estos núcleos inestables tiene una sección eficaz tan baja que su detección en conjunto con la radiación gamma que emiten cuando se desexcitan, con una eficiencia tal que permita acumular una adecuada estadística, es un reto que sólo ha podido enfrentarse recientemente gracias a los últimos desarrollos en las herramientas experimentales de espectroscopía nuclear.

En el año 2011, en las instalaciones del *Laboratori Nazionali di Legnaro*, Italia, núcleos ricos en neutrones con $Z\sim$38 fueron creados usando la reacción de fisión inducida de un proyectil de ^{136}Xe colisionando contra un blanco en reposo de ^{238}U, con una energía cinética de 960 MeV. Para detectar las especies nucleares producidas y la radiación gamma emitida producto de su desexcitación, se usó un montaje experimental compuesto por el nuevo detector gamma AGATA Demonstrator acoplado con el espectrómetro de masas PRISMA. En esta tesis se analizan los datos obtenidos en el experimento para determinar la distribución de masas detectadas para los isótopos de Zirconio y Estroncio, y se obtienen los espectros de radiación gamma asociados a estos núcleos.

Palabras clave: Núcleos ricos en neutrones, deformación nuclear, montaje AGATA-PRISMA, reacciones de fisión inducida (reacciones deep-inelastic).

Abstract

The study of neutron-rich nuclei is currently one of the most active research fields in nuclear physics. The neutron excess that these nuclei contain in comparison to the stable nuclei induces new physics phenomena such as changes of the so called magic numbers given by the nuclear shell model, which leads to unexpected deformations of the nuclear shape of these nuclei far away from the stability line.
In the last decades, neutron-rich nuclei with a number of protons (Z) near 38 have gained attention due to the evolution of their nuclear deformation as a function of the number of neutrons. The most remarkable case corresponds to Zirconium (Z=40), where the nuclear deformation changes from a quasi-spherical shape for ^{96}Zr, to a highly prolate deformation as in the case of ^{104}Zr. Nevertheless, the experimental study of this behaviour has not been completed yet since the low production cross-section of these isotopes demands improved facilities only recently developed, with a detection efficiency high enough to clearly detect these nuclei together with the gamma radiation emmited by them when de-excite.
In 2011, at the *Laboratori Nazionali di Legnaro*, Italy, neutron-rich nuclei in the $Z\sim$38 region were populated by the fission reaction of a ^{136}Xe projectile colliding against a ^{238}U target, at a beam energy of 960 MeV. In order to detect the nuclear species produced and the gamma rays emmited by them, the new γ-ray detector AGATA Demonstrator was used in coupling with the mass spectrometer PRISMA. In this thesis the data obtained has been analysed in order to determine the mass distribution for the detected neutron-rich Zirconium and Strontium isotopes together with their associated gamma spectrum.

Keywords: Neutron-rich nuclei, nuclear deformation, AGATA-PRISMA setup, induced fission reactions (deep inelastic reactions).

List of Content

1 Introduction

Since Rutherford's discovery of the nucleus in 1910 using collisions of alpha particles against thin gold sheets, the knowledge about the nucleus has been substantially improved. The research on nuclear physics carried out during this century has completely transformed human life, not only through its application to vital everyday technologies, such as energy, medicine, and industry, but also through its contribution to our understanding of the physics at distances of just a few femtometers (10^{-15}m).

The nucleus is a quantum system whose main constituents, protons and neutrons, interact via several mechanisms: the strong short-range nuclear force, the weak interaction, and the electromagnetic fields established by the proton charge. The Hamiltonian of this system becomes more and more complex when the number of nucleons belonging to it increases. Some phenomena such as the alignment of angular momenta, the arrangement of shell structures, and collective or single-particle excitation modes take place, determining the value of the nuclear properties which are experimentally measurable, such as life times, total angular momenta, g-factors or, nuclear deformations.

Some "standard" nuclear models -such as the nuclear-shell model- have been used for more than sixty years, predicting with enough accuracy values of experimental observables for the stable nuclei, located in the *stability line* of the nuclide chart, (see Figure 1.1). Usually, these models propose a mean-field potential felt independently by the nucleons (e.g. Woods-Saxon or the Deformed Harmonic Oscillator), in addition to other important interactions like the spin-orbit or angular momenta pairing. The single-particle excitation levels calculated for the nucleons predict a shell structure of the nucleus like the atomic case -despite there is no central potential in the nucleus-. This prediction has successfully explained the observed single-particle behaviour for stable isotopes; as well as the existence of numbers of protons or neutrons with a high binding-energy, known as the *magin numbers*.

A vast majority of the known nuclei have a proton to neutron ratio different from the isotopes belonging to the stability line. In general, they are classified in two groups, a nucleus with a large number of protons than its heaviest stable isotone is called 'proton-rich'; similarly, a nucleus with a large number of neutrons than its heaviest stable isotope is called 'neutron rich', see Figure 1.1. The addition of more nucleons to a stable nucleus changes the dynamics of the system as a whole, modifying the equilibrium of electric and nuclear interactions felt by each nucleon; the nuclei outside the stability region are not stable anymore.

Despite the fact that some corrections can be added to the "standard" nuclear models in order to preserve their applicability to unstable nuclei, different aspects of the nuclear dynamics

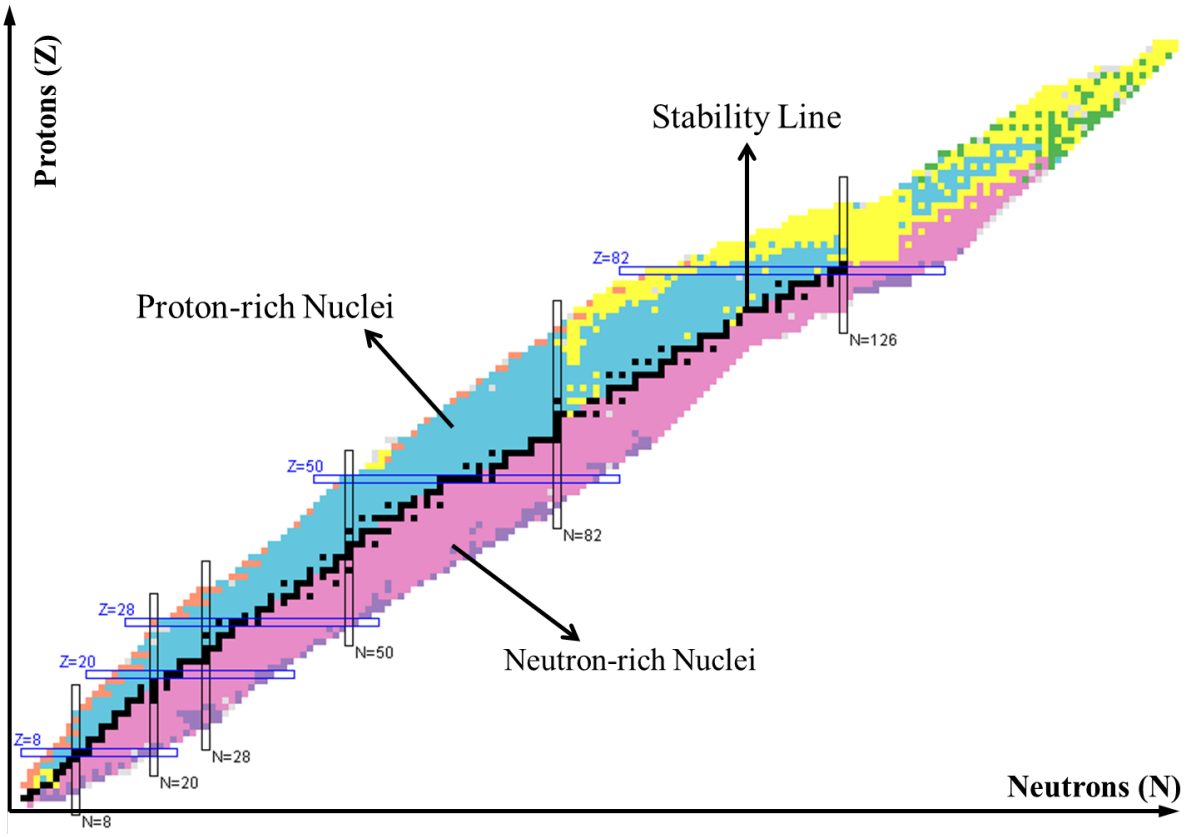

Figure 1.1: Nuclide chart of the isotopes in the nuclear landscape. The stable nuclei, plotted in black, define the region named as *the stability line*. Nuclei outside this region are unstable either with an excess of protons (proton-rich nuclei) or with an excess of neutrons (neutron-rich nuclei). Taken from [1].

exhibited by them remain largely unexplored. For example, the re-arrangement of the shell structure leads to a change in the magic numbers predicted both for proton and neutron rich nuclei; in order to improve the currently limited data on changes in nuclear shells, exotic nuclei far away from the stability line must be produced and studied. In particular, those with a large amount of extra neutrons are currently on the spotlight of the research in nuclear physics.

Neutron-rich nuclei are important to understand nucleosynthesis through the rapid neutron capture process (r-process)[2]. However, they are highly unstable and cannot be naturally found; they must be produced artificially by means of different nuclear processes like nuclear reactions. The population cross section for these isotopes is so low that a suitable and clean identification is a challenge only tackled recently thanks to improvements in the latest experimental facilities.

Over the last decades, neutron-rich nuclei with a number of protons around 38 -referred in this thesis as the "Z∼38 region" of the nuclide chart- gained attention because their nuclear shape changes strongly with their number of neutrons; a remarkable case of this phenomena

is exhibited by the Zirconium isotopes, where the nuclear shape varies from a quasi-spherical low-deformed structure for the ^{96}Zr, to a highly elliptical prolate deformation as in the case of ^{104}Zr [3]. However, a full study of the neighbouring Zirconium region is not complete yet; for example, only in 2011 new information was added to the understanding of ^{104,106,108}Zr [2] and there is still little knowledge about ^{102,104}Sr [1]. Therefore, the execution of more experiments to understand the physics of these nuclei plays a essential role in this research field.

The experiment analysed in this document was carried out in order to explore the nuclear structure of neutron-rich nuclei in the Z$\sim$38 region, by means of the collision of a ^{136}Xe projectile against a ^{238}U target at 960 MeV of kinetic energy. It was carried out at the facilities of the *Laboratori Nazionali di Legnaro*, Legnaro, Italy, from July 1^{st} to July 13^{th} of 2011, using the new γ-array detector "AGATA Demonstrator" coupled with the PRISMA mass spectrometer in order to identify the nuclear species produced during the reaction together with the gamma rays associated with them. As part of a collaboration between different international research groups, several members of the Grupo de Física Nuclear de la Universidad Nacional de Colombia (GFNUN) participated on the experiment. **In this thesis, the data obtained by PRISMA is analysed in order to determine the mass distribution of the Zirconium and Strontium isotopes detected from the reaction; also, the γ-ray energy spectra obtained with the AGATA Demonstrator of these nuclei is obtained**, identifying the lowest excitation energies for several of these nuclei.

In the following sections of this chapter, the relationship between the collective behaviour and the nuclear shape in even-even nuclei will be discussed briefly. Then, the evolution of the nuclear shape as a function of the neutron number in the Z$\sim$38 region will be illustrated, in order to understand the physical problem to be studied. A section about the scope of this work is included at the end of the Chapter. In Chapter 2, two important topics to be considered in the experimental research on nuclear physics are discussed: Nuclear reactions as a tool for populating unstable nuclei, and γ-particle experiments as a technique to study a particular isotope from all the ones produced during the reaction. Chapter 3 discusses about the experiment performed, describing the experimental set-up AGATA-PRISMA, and concludes with a review of several features of the experiment. Chapter 4 explains the data analysis process which leads to the identification of the nuclear species detected during the reaction and Chapter 5 presents the results together with a discussion of them, it is finished with the conclusions for the work performed. An Appendix showing the partial level schemes observed in the experiment for some of the nuclei of interest has been included at the end of this document.

1.1. Collective excitations and nuclear deformation

How can the shape of a nucleus be determined? A many-particle system with just a few fermis of radius cannot be "observed" using classical physics methods. It is through the measurement of the radiation emmited by the nucleus when it de-excites that the information about specific properties such as the deformation of the nuclear shape can be inferred.
In even-even nuclei, all the nucleons couple their angular momenta in pairs so that the *single-particle states*, determined by the independent excitation of one or few valence nucleons, present excitation energies larger than the average binding energy of a coupled angular momenta pair ($\approx$ 2.5 MeV). This quantum states provide information of the nuclear-shell configuration rather than the nuclear deformation. Nevertheless, excited states below this energy have also been detected, being proved that they correspond to coherent excitations of several nucleons [4]. These are known as nuclear *collective excitations*.
In general, the collective state of the nucleus is described by the parametrisation of the nuclear shape. The radial coordinate in the direction (θ, ϕ) at the time t can be expressed as [5],

$$R(\theta, \phi, t) = R_0 \left\{ 1 + \sum_{l=0}^{\infty} \sum_{m=-l}^{l} \alpha_{l,m}(t) Y_{l,m}(\theta, \phi) \right\}, \tag{1.1}$$

R_0 corresponds to the mean value of the nuclear radius deduced from the incompresiblility arguments of the nuclear matter ($R_0 \approx 1.2 \cdot A^{1/3}$ fm). The coefficients $\alpha_{l,m}(t)$ provide the amplitude of the nuclear shape at the multipolar order (l, m). Notice that for the trivial case $\alpha_{l,m}(t) = 0 \; \forall \; (l, m)$, the nuclear shape becomes constant and spherical, which is known as "no-deformed". For different values, these coefficients provide the deformation with respect to the spherical shape at the multipolar order (l, m). Hence, they act as the collective coordinates of the nucleus, being the $Y_{l,m}(\theta, \phi)$ the directional vectors.
Next, it will be shown that the collective modes correspond to the oscillations or rotations of the nuclear shape at the different multipolar orders stated in equation (1.1).

1.1.1. Multipolar deformations

Although Equation (1.1) allows deformations at each possible multipolar order ($l \in [0, \infty)$), there is no evidence of pure deformations for $l \geq 4$ [5]. Hence, only the lowest multipole orders are regarded. These are represented in Figure 1.2.

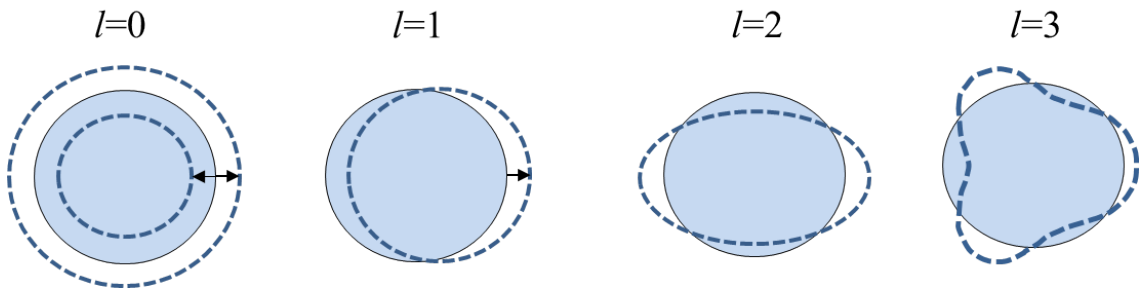

Figure 1.2: Representations of low-order multipole deformations. For simplicity, only the ones that preserve axial symmetry are plotted. The m=0 of the octupole (l=3), which looks like a pear; and the m=0 component of the quadrupole (l=2), representing a prolate ellipsoid.

- Monopole deformation, $l = 0$. It is represented by the spherical harmonic $Y_{00}(\theta, \phi)$, a constant function. This means that a non-vanishing time-dependent value of $\alpha_{00}(t)$ corresponds to a change in the radius of the sphere. The associated excitation is the so-called *breathing mode* of the nucleus. Because of the large amount of energy needed for the compression of nuclear matter, this mode is far too high in energy in comparison to the low energy spectra considered in this work ($E_{exc} \leq 2.5$ MeV) [5].

- Dipole mode, $l = 1$. It is defined by the spherical harmonic $Y_{10} \approx \cos\theta$. Notice that this mode does not correspond to a deformation of the nucleus, but only represents a shift of the nucleus' center of mass, i.e. a translation of the nucleus. Therefore, this multipolar mode is disregarded from our analysis since translational shifts do not modify the state of the system.

- Quadrupolar deformations, $l = 2$. These are the most important multipole deformations because the associated excitation modes are the most common collective excitations of the nucleus. They describe the simplest possible deformations with axial symmetry, the prolate and oblate ellipsoids, which correspond to the m=0 component of the quadrupole (see Figure 1.2). The quadrupolar components with m=$\pm$1, $\pm$2, describe the triaxiality of the ellipsoid shape, i.e. the length difference in the x axis with respect to the y axis, both perpendicular to the axial-symmetry axis of the m=0 component.

- Octupolar deformations, $l = 3$. These are the principal asymmetric deformations of the nucleus associated to collective states with negative *parity* [5]. Only the m=0 component, which looks like a pear, preserve axial symmetry, see Figure 1.2.

1.1.2. Vibrational excitations

The nuclear vibrational excitation is a linear combination of vibrations of the different multipolar shapes mentioned before. In mathematical terms, they correspond to the harmonic

oscillations of the $\alpha_{l,m}(t)$ coefficients around their equilibrium value [4]. Due to rotational invariants, the Hamiltonian describing this phenomena can only be quadratic in the positions $\alpha_{l,m}(t)$, and in the corresponding velocities $\dot{\alpha}_{l,m}(t)$; therefore, it must be expressed as [6]

$$H = \sum_{l,m} H_{l,m} = \frac{1}{2} \sum_{l,m} \left\{ B_l |\dot{\alpha_{l,m}}|^2 + C_l |\alpha_{l,m}|^2 \right\}. \tag{1.2}$$

After a quantisation process for the $\alpha_{l,m}$ and their associated conjugate momenta $\pi_{l,m} = \partial L / \partial \dot{\alpha}_{l,m} = B_l \dot{\alpha}^*_{l,m}(t)$, the introduction of the standard creation-anhilitation operators $O^\dagger_{l,m}$, and $O_{l,m}$ is straightforward; the Hamiltonian then becomes

$$H = \sum_{l,m} H_{l,m} = \sum_{l,m} \hbar\omega_l \left\{ O^\dagger_{l,m} O_{l,m} + \frac{1}{2} \right\}; \quad \left[O^\dagger_{l,m}, O_{l,m} \right] = 1. \tag{1.3}$$

The vibrational collective states can be understood as combinations of excitations between the different (l, m) oscillators in Equation (1.3). The excited states corresponding to the multipolar order l=0 have an energy range very large in comparison with the excitation energy intented to be studied in this experiment, then its contribution to the total Hamiltonian is disregarded. For l=1, the contribution to the Hamiltonian its trivial since this multipolar mode does not produces physical changes in the nucleus state (e.g. it doesn't have excitations). Thus, as a first approximation, only the lowest non-trivial multipole is considered, corresponding to the quadrupolar order, $l = 2$. The Hamiltonian is then approximated as

$$H \approx \sum_{m=-2}^{2} \hbar\omega \left\{ O^\dagger_{2,m} O_{2,m} + \frac{1}{2} \right\}, \tag{1.4}$$

$$H \approx \hbar\omega \left\{ \hat{N} + \frac{5}{2} \right\}; \quad \hat{N} = \sum_{m=-2}^{2} O^\dagger_{2,m} O_{2,m}, \tag{1.5}$$

where $\hat{N}$ corresponds to the number of quanta present in the system. This expression represents five harmonic oscillators, corresponding to each value of m. Each eigenstate of this system has the general form $|N, l, m\rangle$, where N indicates the number of quanta (phonons), l the angular momentum, and its projection m. The first excited states of this system can be deduced by means of successive applications of the creation operators $O^\dagger_{2,m}$ to the ground state, as follows [5]:

- Ground state, $|N = 0, l = 0, m = 0\rangle$. Characterized by zero phonons (N=0), energy $\frac{5}{2}\hbar\omega$, and nuclear angular momentum l=0.

- First excited state, $O^\dagger_{2,m}|0,0,0\rangle = |N = 1, l = 2, m\rangle$. Characterized by one phonon (N=1), energy $\frac{7}{2}\hbar\omega$, and nuclear angular momentum l=2^+. Its degeneracy is given by $-l \leq m \leq l$.

- Second excited state, $O^{\dagger}_{2,m}|1,2,m\rangle=|N=2,l,m'\rangle$. Characterized by two phonons (N=2), and energy $\frac{9}{2}\hbar\omega$. Its degeneracy is given by l=0^+,2^+,4^+; and $-l \leq m \leq l$, for each l.

The level scheme of the lowest excited states of ^{114}Cd predicted by the vibrational model and the comparison with experimental data are shown in Figure 1.3. Despite the good agreement between both level schemes, there are quantitative differences which correspond to the contribution of higher multipolar orders not included in the theoretical analysis explained previously [5].

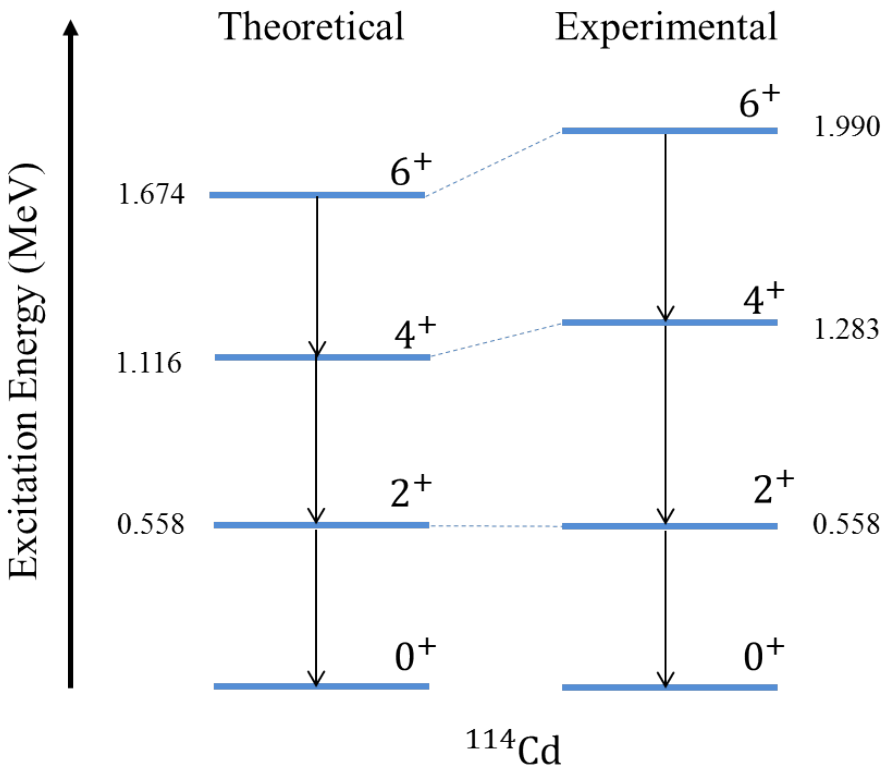

Figure 1.3: Comparison between the theoretical vibrational level scheme of ^{114}Cd with the experimental data [5]. Only the low-energy excited states of interest are shown.

Commonly, when a nucleus decays from a higher to a lower excited state, it releases a γ-ray with an energy equal to the difference of the excitation energy between the involved states. For quadrupolar vibrational excitations, the ratio between the photon energies of the two lowest transition, $E_\gamma(4^+ \rightarrow 2^+)$ and $E_\gamma(2^+ \rightarrow 0^+)$, is given by

$$E4/E2 = \frac{E_\gamma(4^+ \rightarrow 2^+)}{E_\gamma(2^+ \rightarrow 0^+)} = \frac{E(4^+)-E(2^+)}{E(2^+)-E(0^+)} = \frac{(9-7)\hbar\omega/2}{(7-5)\hbar\omega/2} = 1. \quad (1.6)$$

In experimental measurements, some contributions from higher orders excitations can be present, then it is commonly accepted that quadrupolar-like vibrations present an $E4/E2$ near 1.0, 1.4 [2].

1.1.3. Rotational excitations

In a classical mechanics regime a body can rotate about any of its axis, however, in quantum mechanics this is not true. Consider a quantum rotor with no internal structure, when a rotation is applied with respect to one of its simmetry axis then the state of the system doesn't change at all since the enveloping surface remains invariant. Thus, sperical nuclei do not have rotational energy levels and their collective states must correspond to vibrational excitations.

Now, consider a nucleus with the simplest possible deformation, described by an axially symmetric ellipsoid shape, as it is shown in Figure 1.4. Rotations applied with respect to an axis perpendicular to the ellipsoid's axis of symmetry can be clearly distinguished since there is no rotational symmetry in this orientation. Now, if the rotation is applied around an axis tilted an angle α with respect to the symmetry axis, it can be decomposed in a rotation respect to the axis of symmetry, which has no physical changes on the system, and a rotation around an axis perpendicular axis to the axis of symmetry. Therefore, the only possible orientations of the axis of rotation of an axially symmetric ellipsoid are those perpendicular to the axis of symmetry.

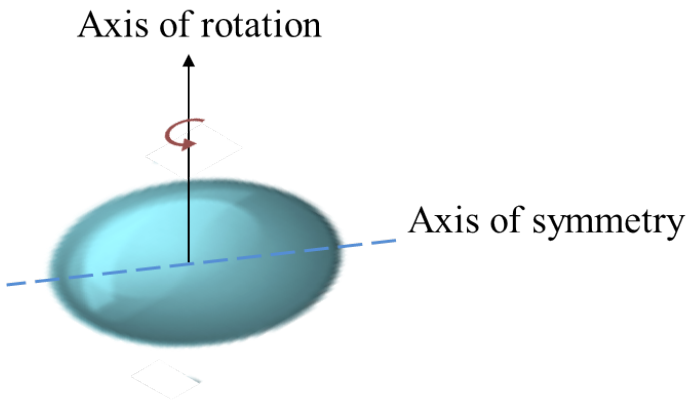

Figure 1.4: Axial-symmetric ellipsoid. When the elongation along the axis of symmetry is greater (lower) than the elongation along its perpendicular plane, the shape is known as prolate (oblate).

Nuclear rotations can be represented by the quantised Hamiltonian of a rotating body with fixed axis,

$$H = \frac{\hat{I}^2}{2\Im} \quad ; \quad E_I = \frac{\hbar^2 I(I+1)}{2\Im}. \tag{1.7}$$

where I=0^+,2^+,4^+.., represent the allowed values of the total angular momentum for even-even nuclei and $\Im$ the nuclear moment of inertia[5]. Since the nucleus is a quantum system, a natural question about the behaviour of $\Im$ in comparison with the moment of inertia of a classical rotor arises. From equation (1.7) the moment of inertia of the nucleus in the

transition between two consecutive states can be obtained:

$$E_I - E_{I-2} = \frac{\hbar^2}{2\Im}(4I-2) \quad \Rightarrow \quad \Im_{exp} = \frac{2I-1}{E_I - E_{I-2}}\hbar^2, \tag{1.8}$$

this expression allows to experimentally evaluate $\Im$ since $E_I - E_{I-2}$ corresponds to the energy of the γ-ray released by the nucleus during the transition $I \to I-2$. The energy of these photons are commonly found in the range of 0.1-1.0 MeV for states with $I \leq 10$ [1], therefore, it can be said roughly that $\Im_{exp} \sim$ 10-25 $\hbar^2$/MeV.
On the other hand, for a classical axially deformed ellipsoid rotating with respect to an axis perpendicular to the axis of symmetry, $\Im$ is given by [7]

$$\Im_{rig.} = \Im_{sph.}\left(1 + \frac{1}{3}\sqrt{\frac{45}{16\pi}}\beta\right) = \frac{2}{5}MR_0^2(1+0.314\beta), \tag{1.9}$$

with R_0 equally defined as in equation (1.1); and the *quadrupolar deformation parameter* β, corresponding to the coefficient $\alpha_{2,0}$ in equation (1.1). Using $M = uA$, with $u = 937$ MeV/c^2, and $\hbar c = 197$ MeV·fm, equation (1.9) can be re-expressed as

$$\begin{aligned} \Im_{rig.} &= \frac{2}{5}\left(937 \text{ MeV}/c^2 \cdot A\right)\left(1.2A^{1/3} \text{ fm}\right)^2(1+0.314\beta) \\ &= 0.0138A^{5/3}(1+0.314\beta) \ \hbar^2/\text{MeV}. \end{aligned} \tag{1.10}$$

From equation (1.10) it can be checked that for nuclei with $A \geq 90$ the predicted moment of inertia under the perspective of a rigid body is $\Im_{rig} \geq$25 $\hbar^2$/MeV, considering β in the common range of 0.0-0.4. This analysis shows that the nucleus does not act as a classical rigid-body since $\Im_{exp} \leq \Im_{rig}$ but as a "soft" rotating body; this happens because not all the nucleons participate in the collecte states of the nucleus but more the valence nucleons on the last shells, nevertheless, this subject is beyond the scope of this document.
Throughout a chain of rotational states it can happen that $\Im$ changes since it is not known whether or not the positions of the nucleons with respect to each other remain independent of the excitation energy. Moreover, taking into account that the nucleus doe not behave as a rigid-body, is suitable to think that $\Im$ does not remain constant. The comparison between the theoretical and experimental spectra of ^{238}U is shown in Figure 1.5.
Considering $\Im$ constant, the ratio between the energies of the photons released in the two lowest transitions, $E_\gamma(4^+ \to 2^+)$ and $E_\gamma(2^+ \to 0^+)$, is given by

$$E4/E2 = \frac{E_\gamma(4^+ \to 2^+)}{E_\gamma(2^+ \to 0^+)} = \frac{[4(4+1)-2(2+1)]\hbar^2/2\Im}{[2(2+1)-0]\hbar^2/2\Im} = 3.33. \tag{1.11}$$

Therefore, if a nucleus with an axially deformed shape presents a rotational-like spectrum its ratio $E4/E2$ must be close to 3.33. Of course, there are many simplifications carried out in this treatment that cannot remain valid in real situations. The shape deformation could have another multipolar contributions and hence the symmetry axes of the system would be

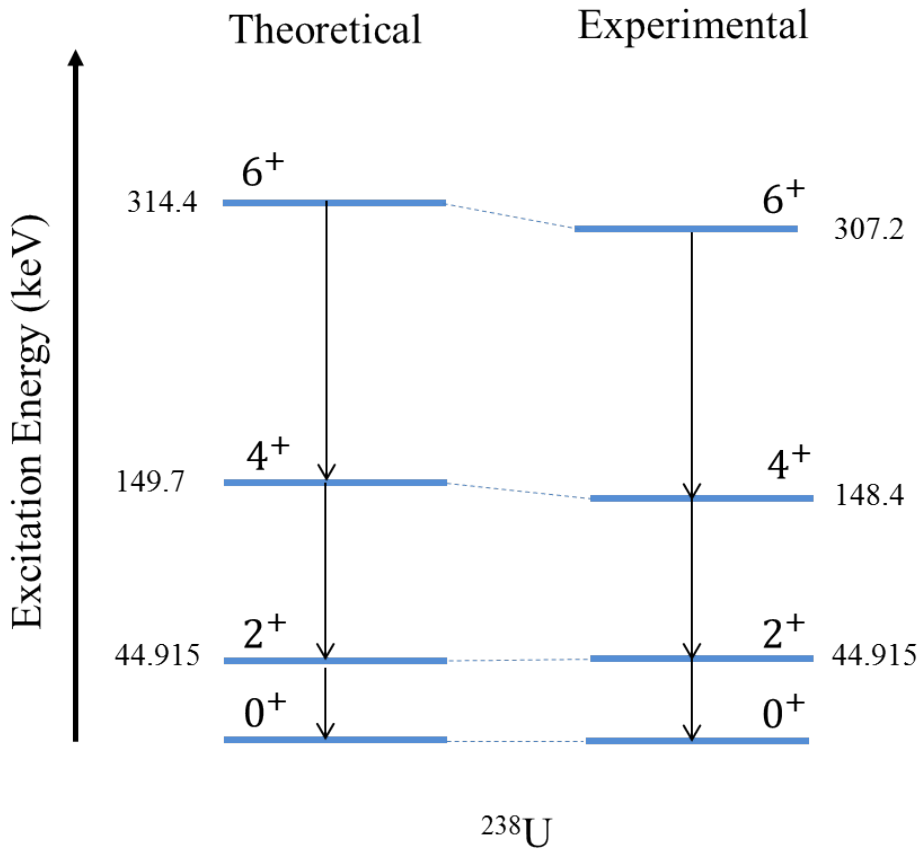

Figure 1.5: Comparison between the theoretical rotational level scheme of ^{238}U with the experimental data [1].

different. Also, if the moment of inertia changes during the de-excitation process, the nucleus is not rigid anymore and "soft" rotors with $E4/E2$ lower than 3.33 may be possible.

1.2. Evolution of the nuclear shape in the Z∼38 region

It has been pointed out by Cakirli and Casten [8] that computing the ratio $E4/E2$ of an even-even nuclei constitutes a simple empirical criteria to determine the kind of collective excitation present, together with the idea about the deformation of its nuclear shape and nuclear shell changes. An $E4/E2$ near 1.0-1.4 is an indication of a spherical shape, meanwhile an $E4/E2$ near 3.3 suggests a quadrupolar one. This criteria has been extensively used to gain an idea of the nuclear deformation in experimental nuclear physics.
Figure 1.6 shows the behaviour of $E4/E2$ for even-even neutron-rich isotopes with $36 \leq Z \leq 44$. For a neutron number N=50 the $E4/E2$ ratio is around 1.5, suggesting collective vibrations and spherical-like deformations. On the other hand, when N rises to 64-66 then $E4/E2$

increases up to 2.7-3.3, suggesting collective rotations of quadrupolar deformed shapes. In every family of isotopes the strongest increment happens at N=58,60; being particularly sharped for the Sr (Z=38), and Zr (Z=40) cases.

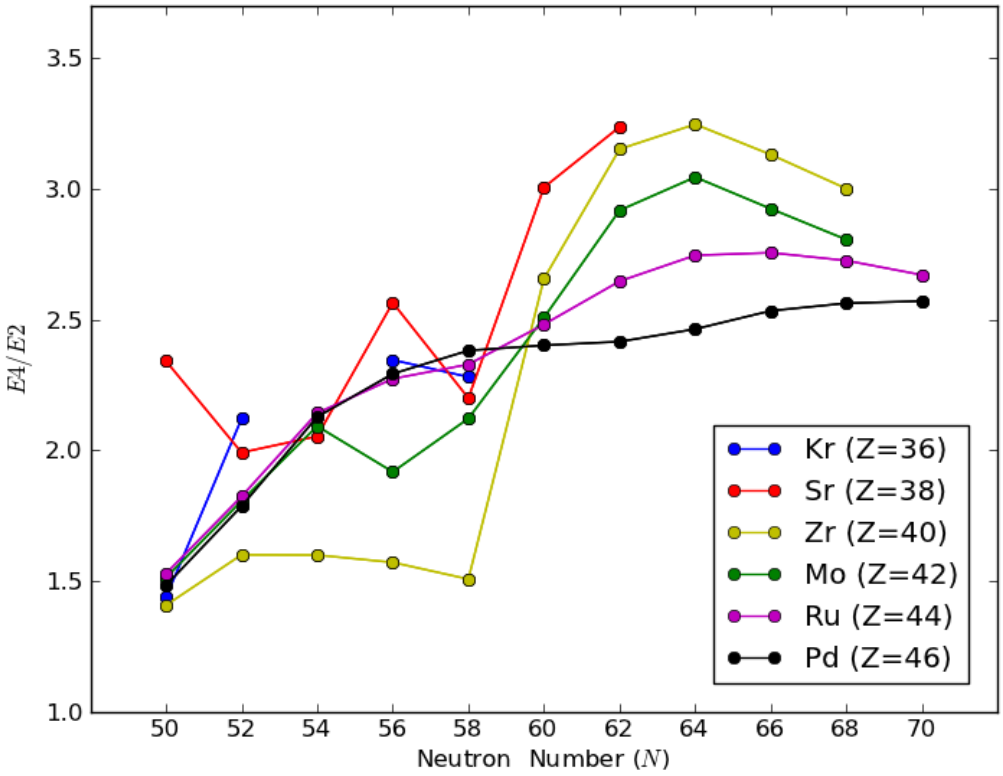

Figure 1.6: $E4/E2$ for even-even isotopes in the $Z \sim 38$ region. Notice the strong variation of the $E4/E2$ ratio before and after N=58, in particular for Sr and Zr isotopes, suggesting a clear strong change in the nuclear deformation.

Actually, Zr neutron-rich isotopes present the fastest shape transition found in the nuclide chart [3], the shape changes drastically from a spherical-like corresponding to a vibrational excitation mode when $N \leq 58$ in ^{98}Zr, to a highly prolate shape characteristic of a rotational excitation in ^{104}Zr, when $N \geq 60$. The quadrupole deformation is known to increase toward $N = 64$ from half-life measurements of the first $I^{\pi} = 2^{+}$ state of even-even Zr isotopes [2]. However, the evolution of the deformation beyond N = 64 is unknown because there is no spectroscopic information. Several authors have predicted different types of shape transition in the neutron-rich region around $N = 70$. Specifically, a ground-state shape transition from prolate to oblate is predicted at $N = 72$ [9] or at $N = 74$ [10]. Furthermore, an exotic shape with tetrahedral symmetry is predicted to be stabilized around ^{110}Zr, which has the tetrahedral magic numbers $Z = 40$ and $N = 70$ [11]. An excited state with the tetrahedral shape, predicted at ^{108}Zr, may become an isomeric state. The tetrahedral shape is still hypothetical in atomic nuclei, in spite of many recent theoretical and experimental works

but there are no direct measurements yet [3].

1.2.1. Scope of this thesis

The experiment to be analized in this work was proposed to complete and extend the spectroscopic information of the neighbouring neutron-rich Zirconium nuclei; in particular, the transitions of the low-lying states for ^{102,104,106,108}Zr and ^{102,104}Sr. In 2011, Sumikama et. al. [2] reported the first 2^+ and 4^+ transitions for ^{106,108}Zr by means of a different population technique, in-flight fission of ^{238}U beams having an energy of 345MeV/nucleon. An independent confirmation of these transitions that can be provided by the experiment performed in this work, since the technique used for probing this neutron-rich region is different. Thus, **the scope for the present work** is to determine the mass distribution of the neutron-rich isotopes of Zirconium (Z=40) and Strontium (Z=38) isotopes detected during the experiment, together with the main gamma-rays associated to each nuclei. Also, some of the transitions recently found in Ref. [2] should be observed provided that there is enough statistics for ^{106,108}Zr. In the next chapter, the physical process to create this nuclei far away from the stability line, as well as the experimental methods to detect them will be discussed.

2 Experimental research of neutron-rich nuclei

In order to investigate the nuclear structure and the physics phenomena that take place inside the nucleus, a large amount of the current experimental research on nuclear physics is dedicated to accelerate a beam of particles such as protons, alphas, or heavy ions, to a desired energy and then collide them against a target of known isotopic composition in order to detect the energy, mass, and scattering angle of the collision products [12]. In general, two conditions must be satisfied to carry out a successful experiment on nuclear physics: An efficient way of populating the nuclei of interest, and an experimental setup with high selectivity and detection efficiency of the nucleus of interest as well as the radiation released when it de-excite. In this chapter the techniques used in the experiment to fulfil both conditions will be outlined, the *deep-inelastic collisions (DIC)* as the mechanism to populate neutron-rich nuclei, and the *gamma-particle coincidences* as the method that allows the identification of the isotopes produced in the reaction.

2.1. Nuclear reactions of heavy ions

The collision of light particles such as protons, alpha particles, or light-ions have been used to investigate some specific excitation modes of the nucleus, namely, single-particle excitations and surface vibrations [12]. This sort of reactions involve just a few nucleons, therefore, the nuclide chart region that can be studied using them is restricted to isotopes with mass numbers near the original target and projectile. The targets available are constrained to stable nuclei belonging to the stability line or close to it[1], far from unstable nuclei such as the neighbouring neutron-rich zirconium region under research in this work.
Nevertheless, the development of facilities with the capability to accelerate heavy projectiles has allowed to explore new regions of the nuclide chart through nuclear reactions of heavy ions. If the energy of the projectile is above the Coulomb barrier of the reaction, both nuclei may fuse and/or fragment in a large number of different nuclear species, allowing the population of wider regions of the nuclide chart far from the stability. Because of that, this kind of reactions are a main tool in the nuclear physics research.

[1] A secondary beam of radioactive isotopes can be produced from the ejectiles of a primary reaction, but usually these beams are not far from the stability line.

The following discussion of heavy-ion reactions is restricted to those with a center-of-mass energy per nucleon lower than 7 MeV, e.g. non relativistic reactions. In this regime, the De Broglie wavelength of the projectile in the center-of-mass system,

$$\lambda = \frac{2\pi\hbar}{|\vec{p}|} = \frac{2\pi\hbar}{\sqrt{2\mu(E - V(r))}}, \tag{2.1}$$

is around 0.5 fm [13]. Let R_p be the radius of a projectile with mass A_p, and R_t the radius of a target with mass A_t. The characteristic dimension ($d_{char.}$) of a heavy-ion reaction corresponds to the minimum distance between the projectile and target when the nuclei slightly "touch" each other, given by

$$d_{char.} = R_p + R_t \approx 1.27 \cdot (A_p^{1/3} + A_t^{1/3}). \tag{2.2}$$

For heavy-ion reactions $A_p, A_t \geq 64$ is typically satisfied, leading to a d_{char} ≈10 fm (For the experiment performed $A_p = 136$, $A_t = 238$ and d_{char} =13,6 fm). Since λ is very small when compared with d_{char}, the diffraction effects of the incident wavelength are not predominant and the movement of the involved nuclei can be described in terms of classical trajectories. In principle, each trajectory is defined by an unique impact parameter, allowing the classification of the different reaction mechanisms according to different impact parameters as it is shown in figure 2.1.
The main processes that take place between projectile and target are:

- **Distant reactions**. These collisions have a very large impact parameter (b_{el}) in comparison with $d_{char.}$, they consist in the **elastic scattering** of the projectile or at most a **Coulomb excitation** of both collision partners. In the Coulomb excitation process the nuclei exchange several quanta of energy through the electromagnetic fields generated by both partners. These collisions do not involve contact between nuclei, so, transference of nucleons is not possible.

- **Grazing reactions**. These collisions take place at impact parameters (b_{gr}) around d_{char} and energies above but near the Coulomb barrier, when nuclei just slightly touch each other. It is accepted that these pheripheral reactions involves just few surface degrees of freedom of both nuclei are involved (e.g. the multipolar orders of equation 1.1), and the transfer of one or two nucleons can happen. In general, only a small fraction of the initial kinetic energy turns into excitation energy [14], giving the alternative name of *quasi-elastic* to these collisions.

- **Fusion-evaporation reactions**. These reactions present the smallest impact parameters (b_F) in comparison to the other possible collisions, being the projectile energy slightly above the Coulomb barrier. Both nuclei fuse in a lapse of time about 10^{-18} s, an interaction time long enough to transform a large amount of the beam energy in excitation energy of the compound nucleus. After the fusion process the average

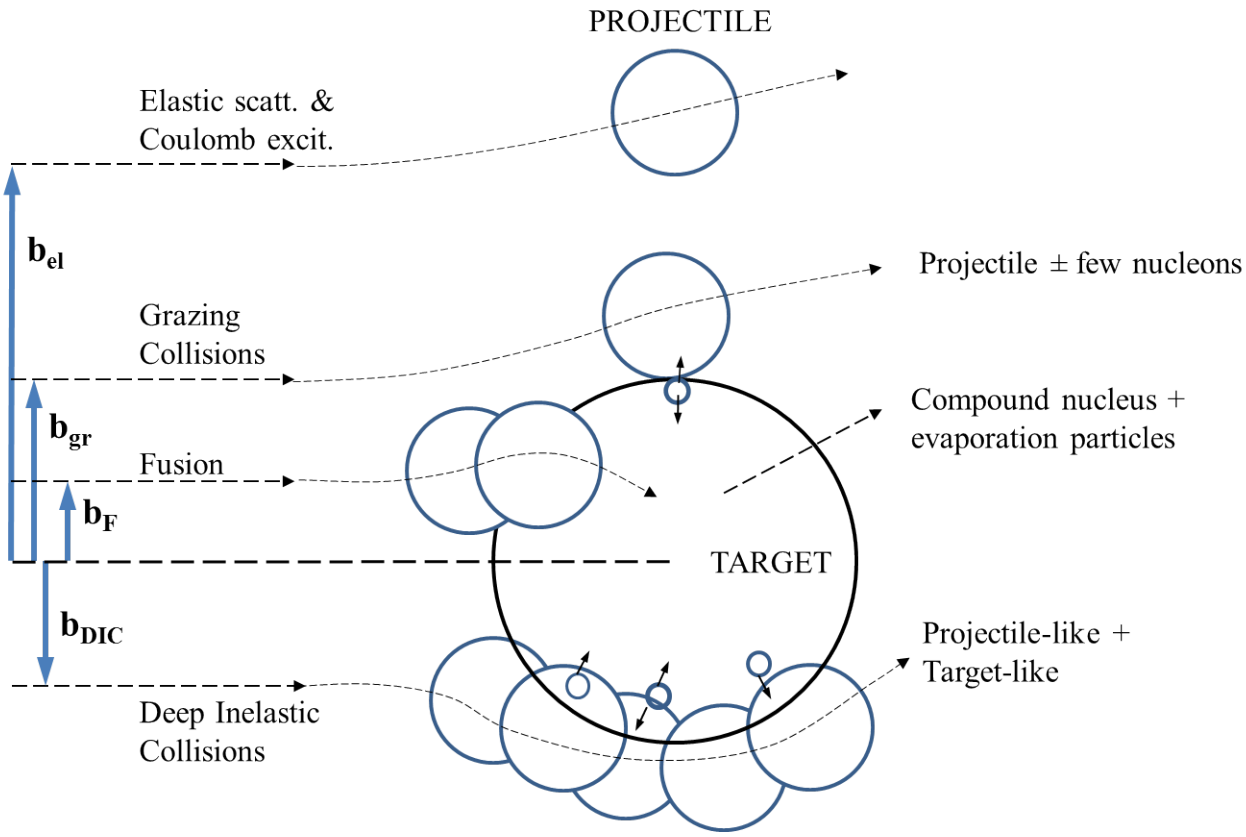

Figure 2.1: Classification of heavy-ion nuclear reactions by impact parameters. Based on [13].

energy per nucleon is usually higher than the bounding energy of the compound system; consequently, the emission of few light particles (n, p, α) to release the excess energy takes place (process known as *evaporation*). The final product is a new isotope in a high-spin state which de-excite releasing γ-radiation, a very suitable condition to perform spectroscopic studies of the nuclear states at very large angular momentum [14]. These type of reactions, together with Coulomb excitation in distant collisions, have been one of the main tools for research on nuclear structure during the last 50 years [10].

- **Deep-Inelastic Collisions (DIC)**. These reactions take place when the impact parameter (b_{DIC}) becomes smaller than b_{gr} but not enough to be within the regime of b_F. The interaction period is shorter than in a fusion-evaporation process, only $\sim 10^{-22}$ s [14]. As the impact between the collision partners is rather peripheral than frontal, they do not overlap completely and keep more or less their identity except for a mutual transfer of nucleons; because of that, the ejectiles can always be identified as *projectile-like* and *target-like*. It must be pointed out that an exact microscopic theory which explains the transfer mechanism of multiple nucleons has not been developed yet because it happens to be very complicated to treat when the number of transferred

nucleons increases [14],[15], these reactions are an open problem that is matter of discussion in ongoing research in theoretical nuclear physics (see [13],[16]). Nonetheless, they are very useful from a practical point of view because they enable the population of isotopes that cannot be obtained with another kind of nuclear reactions, such as neutron-rich isotopes, which are the ones under research in this work.

Of course, the picture previously shown where a unique sort of collision is related to each impact parameter is an oversimplified perspective of the problem. There are fluctuating and frictional forces caused by the particles kinematics inside both nuclei (internal degrees of freedom of the nucleus) which complicates the system. A serious attempt to explain these processes within the frame of Brownian motion and Fokker-Planck equations has been extensively treated by Fröbrich, it can be consulted on Ref. [13]. Due to the fluctuating forces mentioned above, two collisions with identical impact parameters can lead to different final ejectiles, thus, each impact parameter contributes only with a certain probability for the different types of reactions.

2.1.1. Deep-Inelastic collisions (DIC)

The topic of this section can be found extensively discussed in the Chapter 11 of Ref. [13] and Chapter 2 of Ref. [17]. Next, some of the main characteristics of DIC will be outlined, considering the reaction of $^{136}_{54}$Xe with $^{209}_{83}$Bi at E_{CM} = 861 MeV (E_{lab}(Xe) = 1422 MeV). Figure 2.2 shows the contour plot of the double differential cross section $d\sigma/dEdZ$ as a function of the final centre-of-mass energy E and the charge Z of the emitted projectile-like fragments.
From the figure it follows that:

- The large contour plot with $d^2\sigma/dEdZ \geq 0.6$ is centered at the Z number of the beam (Z_{Xe}=54) suggests that most of the times when projectile and target collide remain essentially unchanged except for a few nucleons exchange. DIC can be treated as binary reactions.

- A large number of events with $d^2\sigma/dEdZ \leq 0.4$ present very low final energies. In those cases, a large part of the kinetic energy has been transformed to internal excitation energy. This is the reason why these collisions are called deep-inelastic.

- Although the net mass and charge transfer between the fragments is small on the average, the charge transfer for a given energy loss is not unique, but is spread over a considerable range of values. This establishes that the deep-inelastic reactions are the ones with the highest number of open *channels*, allowing the population of a large number of different isotopes.

An scheme of some of the different projectile-like fragments expected in the experiment performed is shown in Figure 2.3.

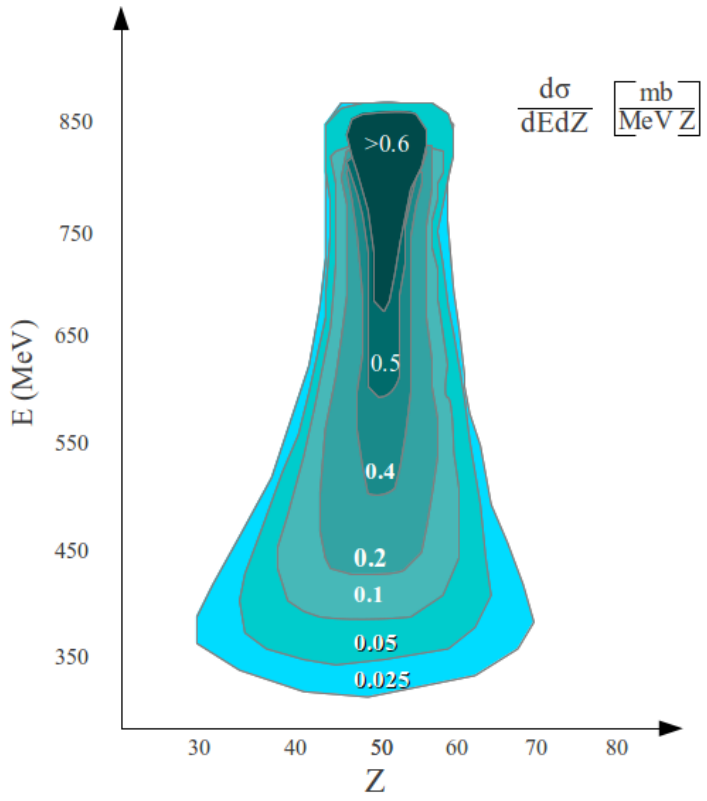

Figure 2.2: Experimental double differential cross section $d\sigma/dEdZ$ as a function of the final centre-of-mass energy E and charge Z of the emitted projectile-like fragments for the $^{136}_{54}$Xe on $^{209}_{83}$Bi at $E_{CM}(\mathrm{Xe}) = 861$ MeV reaction [18].

2.1.2. Grazing Angle of a DIC

Since DIC and Grazing collisions are the lowest cross section reactions, it is important to know the laboratory angle θ_g at which the cross section of these reactions is expected to be maximised. This angle is known as the *grazing angle* of the reaction and is defined as the scattering angle corresponding to the impact parameter when the two nuclei are just "touching" each other. The electronics and equipments used to identify the low cross-section ejectiles must be placed at this direction in order to collect the highest statistics possible. The distance d between the nuclei centers is related to θ_g as it is shown in equation (2.3).

$$d = 1.27 * (A_p^{1/3} + A_t^{1/3}) = \left(\frac{Z_p Z_t e^2}{4\pi\epsilon_0 E_k}\right)\left(1 + csc\frac{\theta_g}{2}\right), \tag{2.3}$$

where $Z_p e$ and $Z_t e$ correspond to the nuclear charges of projectile and target, A_p and A_t stand for the projectile and target mass numbers, and d is expressed in fermis. For the experiment performed, the PRISMA grazing angle is of 48.3°.

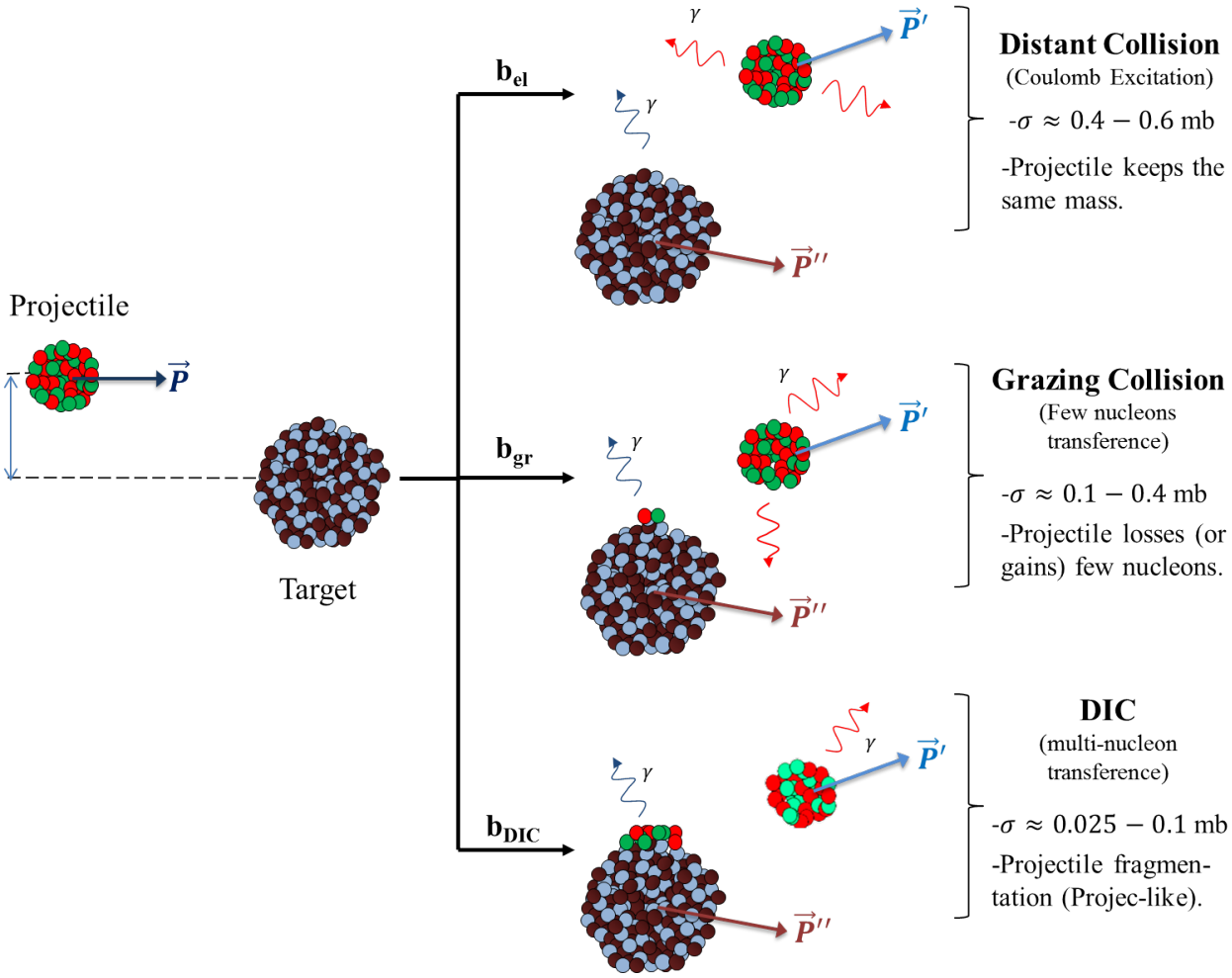

Figure 2.3: Schematic overview of the different collisions and comparison between the ranges of their cross-sections.

2.2. γ-particle coincidences

In the laboratory frame of reference the ejectiles of a nuclear reaction have non-zero velocity and commonly de-excite releasing γ-radiation in flight. The detection of these photons allows nuclear structure studies of the several reaction channels, as for example the deformation of even-even nuclei previously explained in Section 1.2. In order to detect as much radiation from the reaction as possible, high-resolution γ-ray detectors (commonly Ge detectors) are placed near the collision zone. The raw energy spectrum collected by these instruments consists of a histogram of the number of γ-rays detected at some specific energy; since the spectrum records together the transitions from all the reaction channels, it is impossible without additional means to identify which transition corresponds to a particular nucleus. Moreover, the γ-rays emitted by the low cross-section channels have such a low statistic that the corresponding counts in the raw energy spectrum are concealed by the background of the higher cross-section channels (usually, Coulomb and quasi-elastic channels).

In order to study the physics of a particular isotope produced in the reaction it is necessary to assign it the sub-set of detected γ-rays corresponding to the transitions of its de-excitation process. This procedure is known as *γ-particle coincidences*. It consists in colliding the projectile against thin target films so that the ejectiles are not stopped in the reaction chamber but continue on their way until they reach a *mass spectrometer*, a device designed to determine their identity via the measurement of mass and nuclear charge. The signal of the spectrometer when a nucleus is detected is used to trigger a short temporal window in the γ-ray detectors such that each photon detected during this time frame is said to be in coincidence with the identified nucleus. Notice that as the excited nuclear states have mean-lifes on the order of 10^{-15} to 10^{-9} s, a temporal window on the order of 10^{-9}s is large enough to enable the recording of the interactions of all the photons released during the nucleus de-excitation.

As an example, consider the total energy spectrum of the experiment performed (see Figure 2.4 (Top)). Only the Coulomb excitation of both target (^{136}Xe) and projectile (^{238}U) can be clearly distinguished, also the two broad peaks visible at 834 and 596 keV correspond to the de-excitation of the Germanium nuclei of the γ-ray detector after they capture a neutron released in the reaction. Due to the high background, it is impossible from this spectrum to distinguish transitions of a low-cross section channel, such as ^{100}Zr. Figure 2.4 (Bottom) shows the resulting effect on the previous energy spectrum after applying coincidences with the ^{100}Zr channel. The strong suppression of the counts corresponding to photons released by ^{238}U and ^{136}Xe allows a clear identification of prominent peaks that correspond to the transitions of ^{100}Zr.

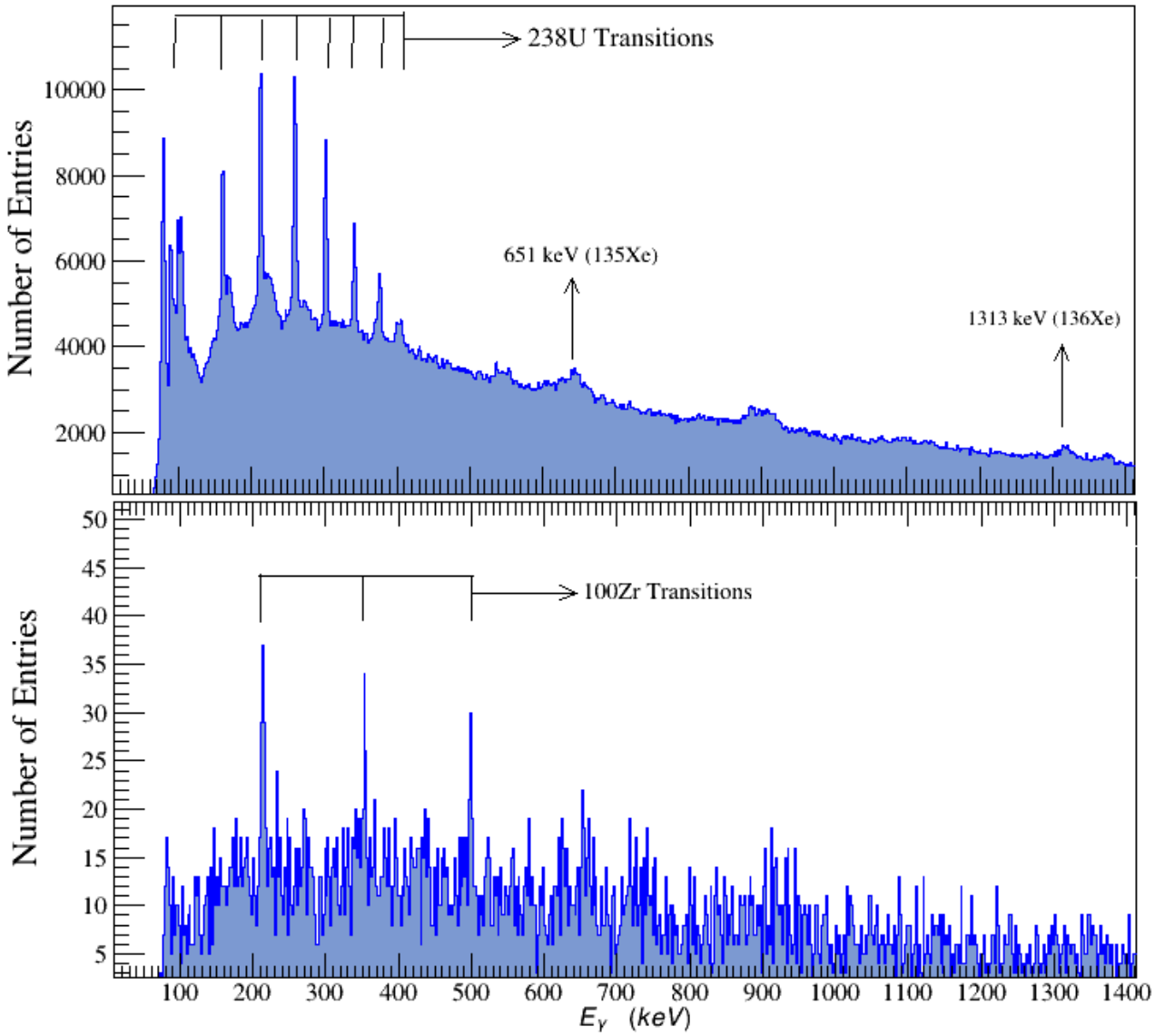

Figure 2.4: Top: γ-energy spectrum of the reaction used in the experiment. Only the photo-peaks corresponding to the Coulomb excitation of nuclei and target are clearly visible since the quasi-elastic channel is the highest cross-section process. Bottom: γ-energy spectrum in coincidence with ^{100}Zr.

3 The Experiment

In this chapter the experiment performed to populate the neighbouring neutron-rich Zirconium isotopes is discussed. It was carried out within the framework of a 2-year experimental campain at the Laboratori Nazionali di Legnaro, Italy, designed to prove the superior capabilities of the γ-ray detector array AGATA Demonstrator when used in real beam time for the first time [19]. Following, it will be explained the experimental setup used to allow for the performance of γ-particle coincidences: The AGATA Demonstrator coupled with the PRISMA mass spectrometer.

3.1. AGATA-PRISMA Setup

The AGATA Demonstrator is a last generation array of γ-detectors, it was coupled with the magnetic spectrometer PRISMA in order to perform γ-particle coincidences for thin-target experiments at the *Laboratory Nazionali di Legnaro*, Italy. This experimental setup was designed to identify and measure the velocity of the ejectiles of the reaction scattered at the grazing angle direction using PRISMA, providing at the same time the energy information of the γ-rays in coincidence using the AGATA Demonstrator. An schematic overview of AGATA and PRISMA positions with regard to the beam direction and the target position is shown in Figure 3.1.

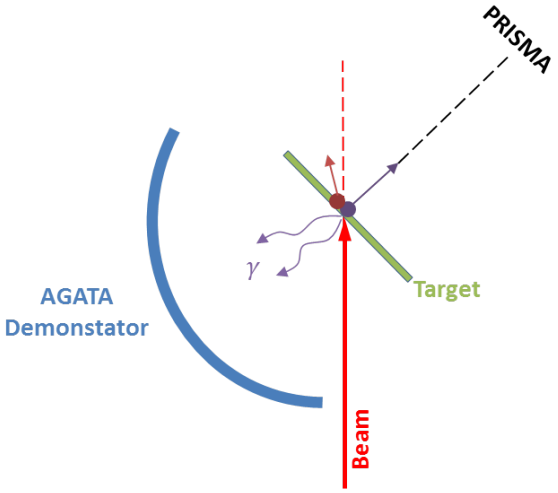

Figure 3.1: Scheme of AGATA-PRISMA setup with regard to the beam direction and the target position.

The ejectiles of the reaction have a velocity relative to the laboratory frame when they de-excite releasing γ-rays, this means that the AGATA Demonstrator measures these photons with an apparent energy shifted according to the Doppler effect, therefore, a correction in the γ-ray spectra is mandatory in order to have the real energy information of the ion's nuclear transitions. This is only possible because the mass spectrometer PRISMA provides the velocity of the emitting ejectile event by event in order to enable a correction via software reconstruction. The AGATA Demonstrator's photo-peak efficiency and the Doppler reconstruction advantages, together with the large solid angle of the magnetic mass spectrometer PRISMA, allow the investigation of the radiation emitted by the weak channels of DIC and Grazing reactions with rather good statistics and precision than its predecessor, the CLARA-PRISMA array [20].

3.1.1. AGATA Demonstrator

The γ-detector array AGATA is a project developed through the last eleven years by a large European collaboration, it is expected to be the first γ-ray spectrometer solely built from segmented germanium detectors covering the whole 4π solid angle. According to simulations, it is expected to have a photo-peak efficiency of 50 % at 1 MeV energy, being the most advanced and efficient γ-detector array ever developed [21]. The main difference of this detector array in comparison to previous ones, such as CLARA or GAMMASPHERE, is the possibility of tracking the photon's trajectory inside the detectors, using the Pulse-Shape-Analysis technique [22], improving the absolute photopeak efficiency to 2-3 orders of magnitude while preserving the extremely good energy-resolution of the germanium detectors.
Since the project is currently at its initial phase, only a subset of the array known as the AGATA Demonstrator has been built. It is composed of five triple clusters of segmented Ge detectors (i.e. giving a total number of 15 crystals). Each crystal is composed in turn by 36 segments, which give an overall number of 540 segments, see Figure 3.2. The data acquisition system (DAQ) limited the counting rate of each crystal to a maximum of 1.5 kHz, approximately to 1 GB/min. However, the detection of environmental radiation which is not of our intereset can generate much of this data, therefore, an aproppiate trigger system must be present in each experiment in order to record mostly data of interesting events. The relevant information about the AGATA Demonstrator during the experiment is summarised in Table 3.1.

Solid angle covered	$\approx 0.3\pi$ sr
Target distance	20.2(1) cm
Photopeak-efficiency	≈ 6 %
Temporal coincidence window with PRISMA	3μs

Table 3.1: Experimental parameters for the AGATA Demonstrator during the experiment.

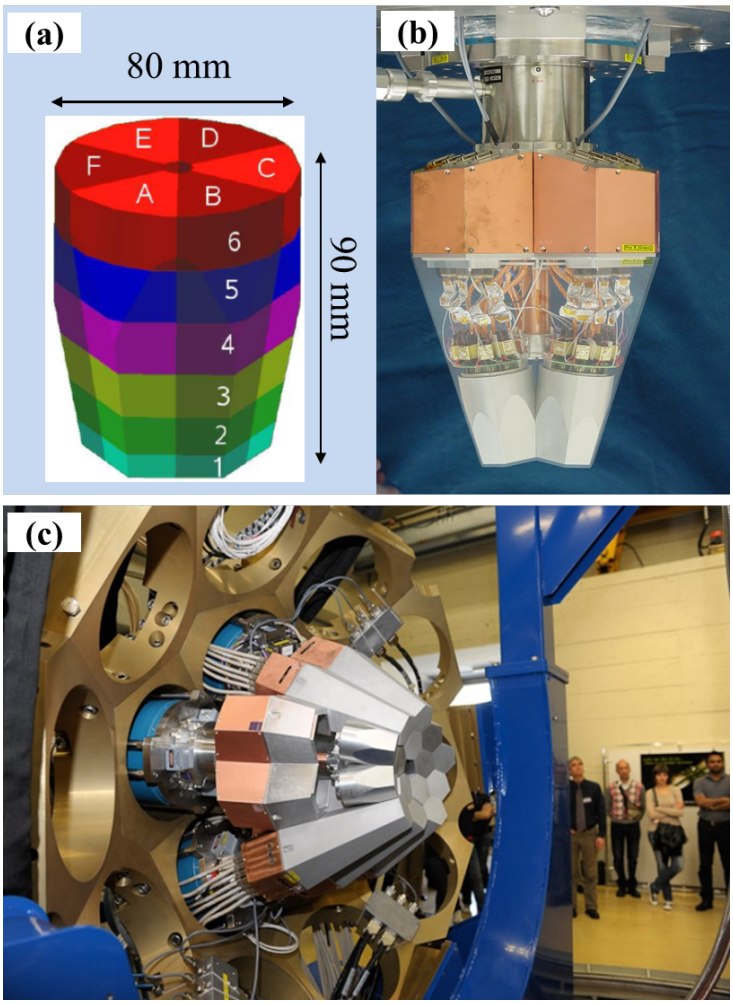

Figure 3.2: (a) Scheme of a single Ge segmented crystal [23], each segment is labeled as A1, A2, etc. (b) A cluster of Ge detectors connected to their corresponding electronics with 3 crystals. (c) AGATA Demonstrator with 5 triple-clusters at LNL [21].

3.1.2. PRISMA

PRISMA is a magnetic mass spectrometer designed to provide the nuclear charge Z, and mass A, of the ejectiles from nuclear reactions with heavy ions, its development and construction was performed at the *LNL* facilities, from 2000 up to 2003. PRISMA provides event-by-event information needed to identify ejectiles of a nuclear reaction via the examination of mass, atomic number, charge state, velocity, and kinetic energy for each detected isotope. It is usually located at the corresponding reaction's grazing angle in order to collect higher statistics for the low cross-section channels in comparison to other angular positions, as it was explained in Section 2.2.1. One of the main PRISMA features is the large solid angle detection it has in comparison to other magnetic mass spectrometers [24]. It is essentially divided into five sections, a general scheme is shown in Figure 3.3.

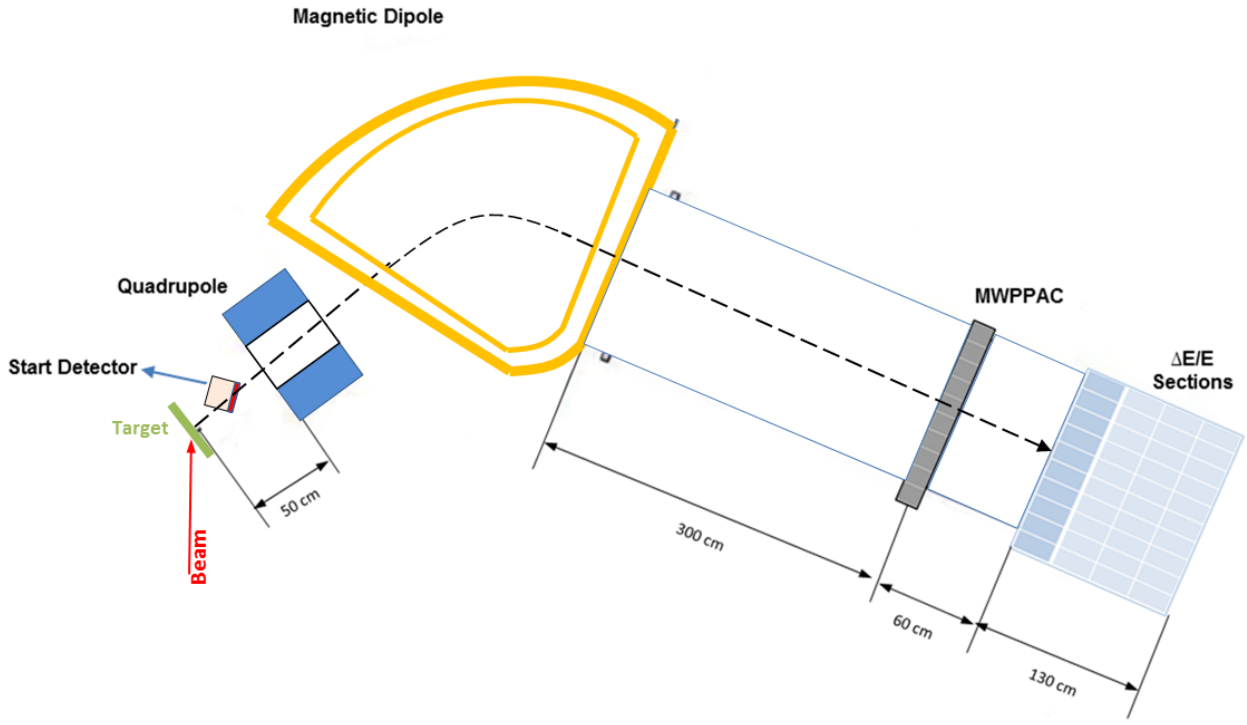

Figure 3.3: Top schematic view of the PRISMA spectrometer. The black line represents the central trajectory of an ejectile inside PRISMA when it is scattered from the target in the θ_g direction.

When the nuclei reach PRISMA they cross through the **Start Detector**, where their entrance (X,Y) position and time are measured. They continue and quickly reach a **Magnetic Quadrupole** which generates a magntic field designed to narrow down the distribution size along the vertical position (Y), focusing the incoming ions at the horizontal plane Y=0. They continue and reach the **Magnetic Dipole**, a semi-circular region where a constant vertical magnetic field is established forcing each ion to perform a semi-circular trajectory with a radius according to its own mass over charge ratio. The ions leave this region with their trajectories separated and then reach the **MWPPAC**, where position and time signals are measured again in order to use them together with the start detector signals to compute the ion's time of flight (TOF), trajectory's length, and consequently, their velocity. Finally, nuclei are stopped when once they reach a large segmented array of gas-filled ionisation chambers (**ΔE-E detectors**) where their kinetic energy is measured. The process to identify each nuclei detected using the signals measured by PRISMA is the main subject of the next Chapter. First, the details about the experimental sub-systems mentioned above will be provided following in order to understand the capabilities and limitations of the mass spectrometer.

The start-detector

The start detector is placed at 25 cm from the target, see Figure 3.4. It consists of a rectangular Micro-Channel-Type detector (MCP) with an area of 80×100 mm^2 designed to detect positions of charged particles almost with 100 % efficiency [25]. However, the MCP is not directly placed at the PRISMA's entrance because it would stop the ejectiles coming from the reaction chamber, instead, only a very thin carbon foil is placed there, tilted 45° with respect to the PRISMA's optical axis (i.e. the central trajectory). The ions cross through the foil without measurable alterations of their trajectories, and at the same time they ionize the carbon atoms. The electrons taken out are conveyed towards the MCP using an electric and a magnetic field stablished by grids covering the foil and two external coils respectively (see Figure 3.4). The fields are designed so that the electrons are accelerated straight towards the MCP preserving the ion's position information. A temporal signal is registered when the ions cross through the foil with a temporal resolution of about 130 ps. Figure 3.4 shows an schematic view (from above) of the start detector.

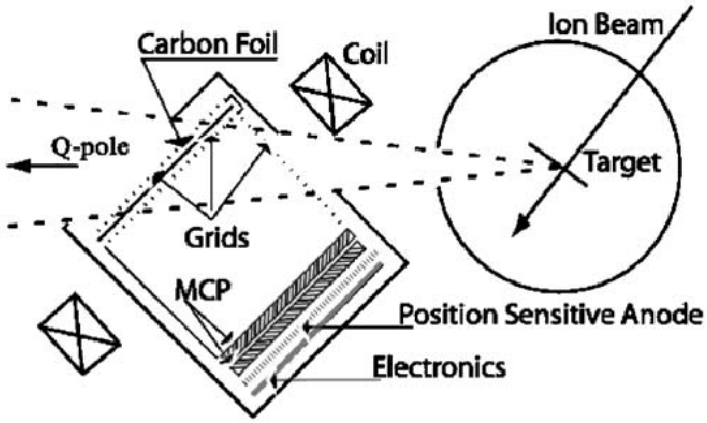

Figure 3.4: Schematic overview of the start detector setup, taken from [25].

The micro-channel plate MCP is an array of miniature electron multipliers tubes, parallel oriented each other. When a charged particle hits a particular tube, a cascade of electrons is generated inside due to the bias voltage of the MCP. All the charge produced is collected by a position sensitive anode with a resolution of the order of 1 mm, therefore the Start Detector's resolution is around 1 mm both X and Y. In fact, PRISMA uses two MCP in quasi-parallel positions, this is known as the *Chevron configuration* and is used because it increases the charge recollection by many orders of magnitude [25].
Summarizing, the Start Detector provides:

- The entrance position (X,Y) of an ejectile when they cross through carbon foil with a resolution in the order of 1 mm^2 [25]. These signals will be used to reconstruct each ion trajectory.

- The *start time signal* with temporal resolution of around 130 ps, it will be used to measure the time of flight (TOF) of the ejectiles.

The Focusing Quadrupole

The Magnetic Quadrupole is placed 50 cm straigth after the target and has an active diameter of 30 cm and an effective length of 50 cm, its function is to focus the ions onto the vertical plane (x-y) shown in Figure 3.5.

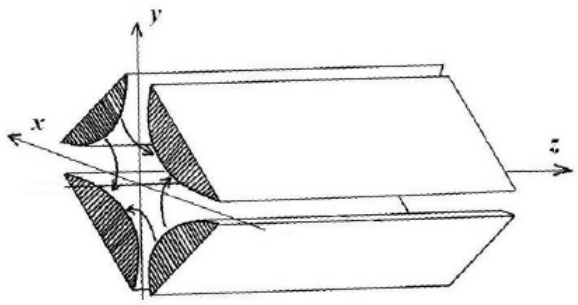

Figure 3.5: Focusing Quadrupole of PRISMA spectrometer, taken from [14].

The z-axis in direction of PRISMA's optical axis is defined with x and y as shown in Figure 3.5, with the origin in the center of the focusing quadrupole xy plane. The Quadrupole's magnetic field has two components [14]: $B_x = by$ and $B_y = -bx$, with b a positive constant. Consequently, the forces acting on an isotope with a charge state q are: $F_x = -qv_zB_y = qv_zbx$ and $F_y = qv_zB_x = -qv_zb$y. It can be seen that this force always acts in the direction $(x, -y)$, thus the net effect is the reduction of the distribution size of ions along the y axis and the increase of it along the x axis.

Magnetic Dipole

After the focusing quadrupole, the ions go on towards the Magnetic Dipole, a semicircular region with a constant vertical magnetic field, perpendicular to the ion's motion plane. The Lorentz force acting on the ions is then given by

$$F = ma \Rightarrow qBv = \frac{mv^2}{R} \Rightarrow \frac{mv}{q} = BR \Rightarrow R = \frac{mv}{qB} = \frac{\rho_m}{B}, \tag{3.1}$$

with q the ion's charge state, B the strength of the magnetic field produced by the dipole, and R the radius of the ion's circular trajectory. Equation (3.1) states that ions with different **magnetic rigidity** ρ_m have a different associated radii R, therefore, after crossing the magnetic dipole, the isotopes have different trajectories depending on their charge state and momentum. This separation is the main purpose of the Dipole, its main characteristics are summarized below:

- Bending radius R ∼1.2 m in the center.
- The angle between the direction of entrance and exit is 60°.
- Maximum magnetic field available B ∼1 T.
- Magnetic rigidity $\rho_m = BR$ ∼1.2 Tm.

It is proved that a semi-circular magnetic dipole focuses the trajectories of ions with the same energy but different entrance angle in horizontal direction. In other words, it behaves like a lens [14] with the object and the image placed in the same line that crosses the Dipole's vertex circle, as shown in Figure 3.6. The net effect is that the ions are focused in different regions of the focal plane because of their energy, this is where PRISMA gets its name from.

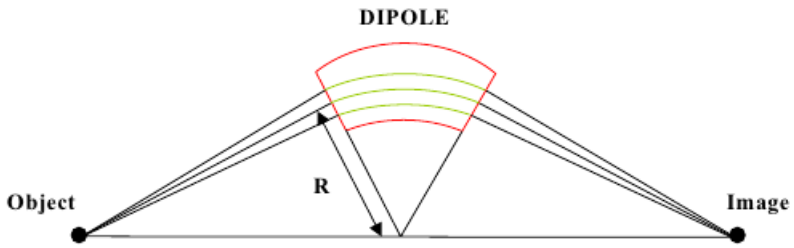

Figure 3.6: Scheme of circular-shape magnetic dipole operating as a lens. Taken from Ref. [14].

MWPPAC

The PRISMA focal plane is located 300 cm after the magnetic dipole. In this position, a MWPPAC (Multi-Wire Parallel Plate Avalanche Counters) detector is placed. It has a large sensitive area of 100×13 cm^2, providing x, y positions and the *stop-time signal* for the ejectiles coming from the Magnetic Dipole, see Figure 3.7.

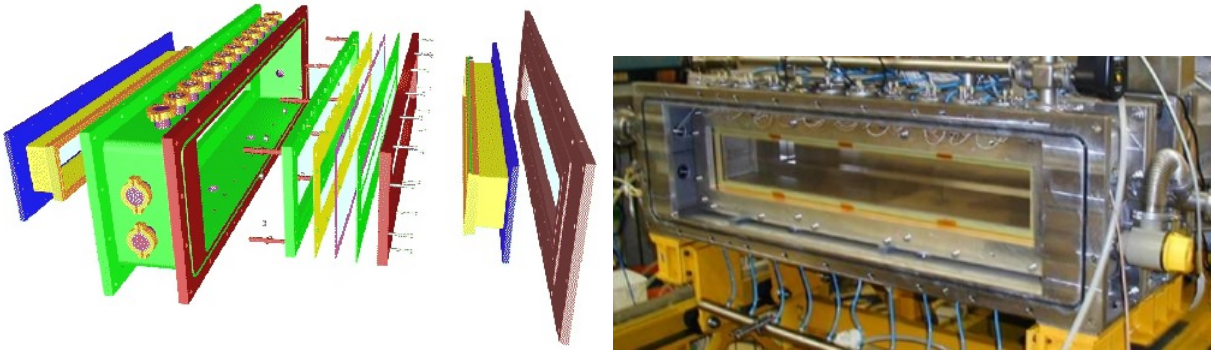

Figure 3.7: PRISMA's MWPPAC Detector, taken from [24].

This paragraph is largely based on [15]. The MWPPAC is made up by 10 independent sections of 10 cm placed adjacent to each other. The structure of each one is composed

of three electrodes; a central cathode (a wire polarized at high voltage) for timing, and two anodes at ground potential with respect to the cathode, composed by two wire planes oriented ortogonally to each other, located 2.4 mm away in the z-direction from the cathode to provide the (X, Y) position of the detected nucleus. The X-position sensitive wires are distributed over 1000 mm with a step of 1 mm, each wire provides a position signal using the delay-line method, hence one has two signals from each section, whose relative delay is proportional to the position of the incoming ion. The cathode is made by a plane of wires divided in 10 sections, like the X wire plane. All the electrodes are mechanically connected to each other and then fixed on the vacuum vessel. Two 200 μg/cm^2 Mylar windows separate the MWPPAC gas volume from the rest of the spectrometer. The experimental data provided by the MWPPAC is summarized following [14],[26]:

- *Stop signal* used together with the *start signal* to obtain the time-of-flight TOF (resolution of 300-400 ps).
- Focal plane position (resolution of 1 mm in the x, and 2 mm in the y axis).

ΔE-E detectors

An array of ionization chambers (IC) constitutes a ΔE-E system of detectors whose main functions are to distinguish between ions with different atomic number Z and measure their kinetic energy. With the purpose of exploiting PRISMA's large solid angle acceptance, the IC array has a considerable area, $100(x)\times20(y)$ mm^2, and an active depth of 120 cm. With these dimensions it is expected that all ions are stopped, because the ionization range is long enough even for heavy ions, with high kinetic energy, to be halted. The distribution of the array consists in 10 adjacent ΔE-E detectors, each one composed by 4 IC slots (see Figures 3.3 and 3.8). The filling gas is methane with 99.9 % purity, selected for its high electron drift velocity.

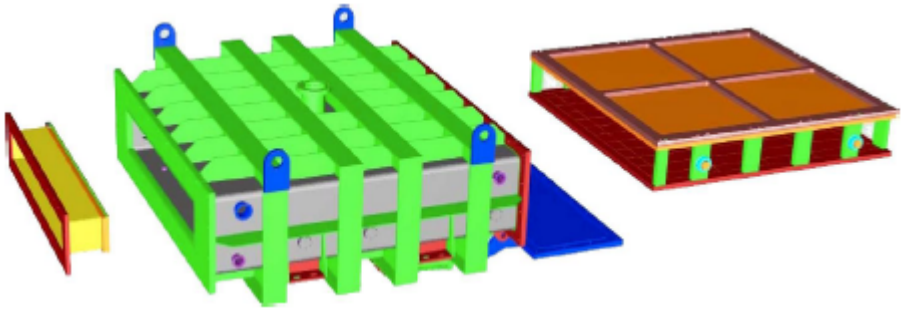

Figure 3.8: Schematic view of the IC array: Electrode package (right), the stainless-steel vacuum vessel (centre), and the entranced window (left) , taken from [24].

The information provided by the ΔE-E detectors array is summarized following [14],[26]:

- Nuclear charge, resolution adequate to distinguish Z up to 60 at energies 2-10 MeV/amu.
- Kinetic energy of the detected ejectiles.

3.2. Review of the experiment

3.2.1. Target and beam descriptions

Target

A thin ^{238}U film covering an area of around 3.0 cm^2 was used as target, it is supported on a carbon backing in order to have mechanical stability. The density of the U-film is about 19.1 g/cm^3 and the melting point is 1132 °C.
During the experiment, the beam current sometimes presented instabilities reaching a higher value than expected, in those cases it transfered enough energy to the target to melt it, piercing the film. Because of that, 6 different replacement targets with the same composition were used, their thickness specifications are summarized in table 3.2.

N°	^{12}C (μg/cm^2)	^{238}U (μg/cm^2)
1	42	989
2	43	1011
3	41	1045
4	40	1017
5	39	1017
6	43	966

Table 3.2: Thickness of the targets used during the experiment. Notice that Uranium films are by far thicker than the carbon backings where they are supported.

It is important to notice that a *thin target* does not neccesarily has a short longitudinal length, what it actually means is that the target's number of scattering centers is short enough in order not to stop the beam. As the total stopping power of the target depends on its density and transversal-lenght, the *thickness* is given in units of density per length (ρ·cm) or, mass per area (μg/cm^2).

Beam

The beam was composed of stable $^{136}_{54}$Xe ions accelerated at 960 MeV provided by the Legnaro PIAVE+ALPI accelerator complex at LNL, it was produced by the electron cyclotron resonance source of PIAVE, preaccelerated, injected in the ALPI-Booster, and accelerated up to the final kinetic energy, with an initial charge state (i.e. the difference between its number of protons and electrons) of +28. The energy per nucleon is around 6.23 MeV, below the relavistic regime of 7 MeV mentioned in Chapter 2. Xe ions moved with a velocity given by,

$$v = \sqrt{\frac{2E}{m}} = \sqrt{\frac{2 \cdot 960 \text{ MeV}}{135.907 \text{ a.m.u}}} = \sqrt{\frac{2 \cdot 960 \text{ MeV}}{135.907 \cdot 931 \text{ MeV/c}^2}} = \sqrt{0.0151}\text{c} = 0.1\text{c}. \tag{3.2}$$

During the experiment, the beam current's intensity fluctuated between 0.5-2.5 pnA, corresponding to an electrical current between 14-70 nA. The "pnA" unit stands for *particle nanoampere* and is defined as the electrical current divided by the charge state of each particle, in other words, it expresses the beam's number of particles per second.

For a constant beam intensity the target temperature increases when the spot size of the beam decreases. This can happen when the acceleator conditions become unstable and the beam is focused on a smaller area, increasing the power (energy/area) released on the target. If the temperature surpasses a critical value the target melts, therefore it is important to have an idea of the temperature induced by the beam at different currents and spot-sizes. A table with the different target temperatures depending on the beam spot radius and intensity is shown below.

Beam current (pnA)	Beam spot radius (mm)	Target temperature (°C)
2	1.0	1657
2	2.0	1252
2	2.5	1122
3	2.5	1674

Table 3.3: Target temperatures for some typical values of beam current and beam spot radius. These values must be compared with the target melting temperature, about 1132 °C.

3.2.2. Beam's performance

For nucleus created through mechanisms of Deep Inelastic Collisions is important to determine an appropriate beam energy value that keeps the excitation energy of the compound nucleus as low as possible in order to minimize pre-fission neutron emission whilst maintaining a usable cross section [3]. The optimal value is experimentally adjusted finding the beam energy that maximises the production of neutron-rich nuclei. It was expected to use two of the thirteen days of beam-time for setting up the ideal beam energy, and 11 days for collecting data of the Z∼38 region. The beam was expected to be scanned for energies between 900 and 1050 MeV, with a 2-3 pnA intensity current.

However, it was not possible to scan the beam's conditions since there were some problems with the ion source supply [27]. The behaviour of the beam current throughout the experiment is summarized as follows: The average current remained below 2 pnA, in 5 occasions there was no beam for 4 hours and once the beam was off during 11 hours [27]. In short periods of time the current grew above 3 pnA breaking three of the targets available, causing holes and a mechanical deformation of the film.

3.2.3. Amount of data collected

Given the beam conditions described before, the number of collisions ocurred during the experiment was less than expected due to the beam's low current, therefore, the amount of data collected will be decreased. The following calculation is performed in order to stablish a comparison between the real data collected versus the expected one.
After reviewing the experiment's logbook, a set of *runs* (data files) that registered high counting rates of the PRISMA detectors and relatively high and stable beam conditions is chosen; then it was selected the one with the highest number of Zirconium counts:

File	Number of Zr events	Measurement time	Events/hour
run_0029	4497±68	4 hours	1118±33

This run can be used as a reference to estimate the ideal number of Zirconium events that were ideally expected. If the conditions of this *run* would kept constant during the whole experiment (13 days), the total collected statistics would be

$$\textbf{Zr events} \rightarrow \textbf{Time (h)}$$

$$1118 \pm 33 \rightarrow 1$$

$$\text{Total Zr events} \rightarrow 24 \times 13$$

$$\text{Total Zr events} = \frac{1118 \times 264\text{h}}{1\text{h}} = 348816 \pm 590.$$

Nevertheless, the total counts of Zr events is only 235602±485, this corresponds to 65.7 % of the expected data, or 8.7 days of beam-time with optimal conditions.

4 Data Analysis

In this chapter the data analysis carried out to perform the identification of the detected nuclei is discussed. The data analysis was largely conducted using ROOT [28], a programming tool massively used by the nuclear and particle physics community, created at CERN to improve the analysis of large-data experiments. Also, the GammaWare software [29] was used in order to process the raw data and create *Trees*, the adequate input data structures to be analized using ROOT. Each time when PRISMA detects a nucleus all the information listed below is provided by its detectors and stored as a single **event**:

- Entrance position (MCP_x, MCP_y): Position of the nucleus when it crosses the Start Detector carbon foil.
- Time of flight (TOF): Time used by a nucleus to travel from the Start Detector to the MWPPAC.
- Focal plane position (X_fp): Horizontal position of the nucleus when it reaches the MWPPAC, located at PRISMA's focal plane.
- Length (D): Length of the trajectory described by the detected nucleus from the Start Detector to the MWPPAC.
- Radius (R): Radius of the circular trajectory described by the nucleus inside the magnetic dipole.
- Kinetic energy (E): Total energy lost by the nucleus in the the array of ionization chambers.
- ΔE: energy released by the nucleus in the first two segments of the ionization chamber array.
- A/Q: Ratio between the mass number, A, and the charge state, Q, of the detected nucleus.
- GammaE: Set of γ-ray energies measured by the AGATA Demonstrator for all the photons in coincidence with a nucleus detected by PRISMA.

The stategy to identify a nucleus is shown below:

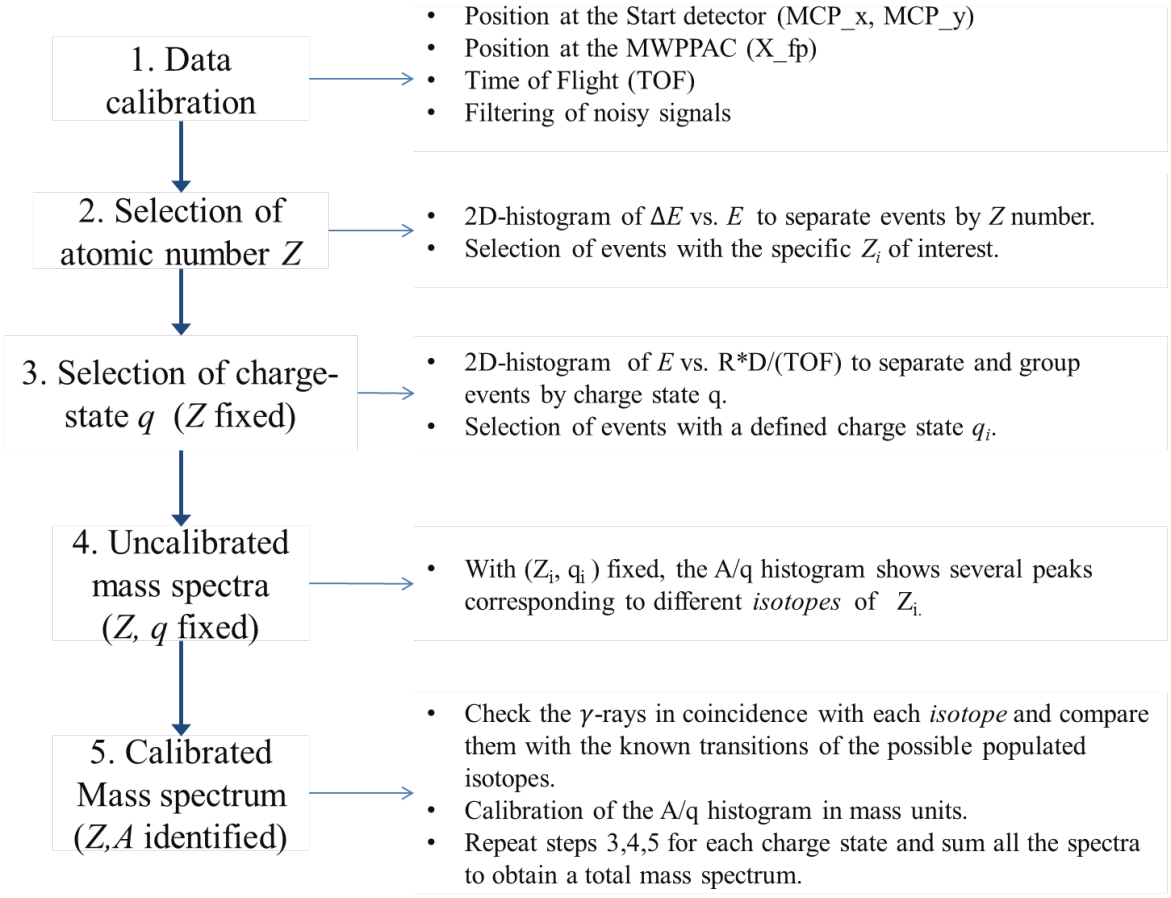

4.1. Data Calibration and filtering

4.1.1. Start Detector spectrum

The Start Detector spectrum is a two-dimensional histogram of the (x, y)-position of the nuclei when they go through the carbon foil; the number of counts registered in each bin are plotted using a colour scale, the associated colour code is shown at the right side of the histogram plot, see Figure 4.1. The data acquisition system has been set so that only the ions that reached the MWPPAC were recorded, therefore, only the events shown in Figure 4.1 fulfilled the logical "AND" condition set between the MCP and MWPPAC signals [15]. The Start Detector spectrum provides an idea of the spatial input distribution of the ions arriving to PRISMA; some are stopped in a cross with four small nails (points of reference) placed just behind the carbon foil and do not generate a signal in the MWPPAC, because of that, a low-count cross-shaped region is created in the histogram. This "shadow" is used as a reference frame to perform the spatial calibration of the Start Detector spectrum; an adequate calibration is obtained once the nails' position are alligned both vertical and

horizontal, and the cross' center coincides with the PRISMA's central trajectory which is placed at the entrance position $(0, 0)$. It can be seen in Figure 4.1.

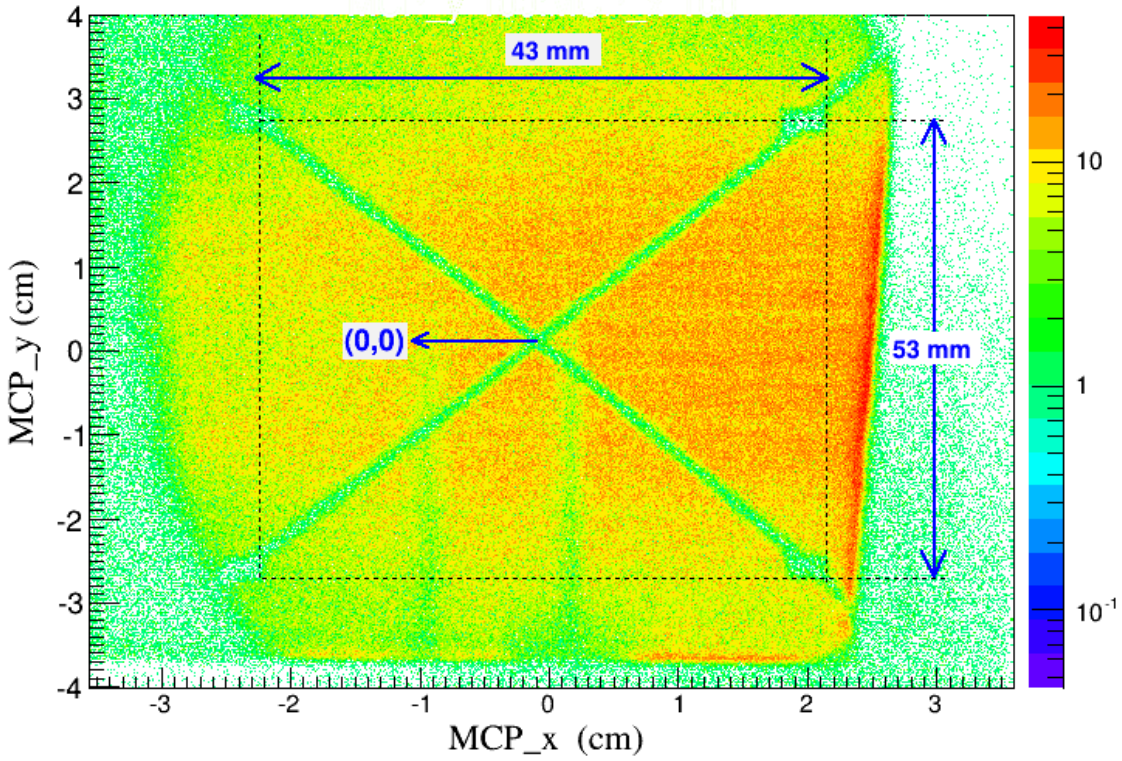

Figure 4.1: A typical calibrated MCP spectrum, the allignment of the cross reference points can be seen, both vertical and horizontal.

Figure 4.1 shows the spatial input distribution of the ions detected by PRISMA. The highest-count region, a slightly-tilted vertical red zone placed between 2.4 cm ≤MCP_x≤ 2.6 cm, corresponds to noise signals of the MCP detector and must be excluded from the analysis, thus only events that fulfill the condition -2.5≤MCP_x≤2.3 and -3.5≤MCP_y≤3.5 are regarded. The two green vertical blurry shadows placed at MCP_x=-1, and MCP_x=0, correspond to a pair of nails fixed at the end of the magnetic quadrupole.

4.1.2. MWPPAC Spectrum

Each one of the ten MWPPAC sections provide an independent X_fp signal which is recorded in a standard output histogram within the range from 0 to 8191 (channel units). Nevertheless, each section covers 100 cm of the focal plane, thus the range of the associated histogram must be calibrated and rebinned adequately in length units. After this process the ten sections are displayed together in a single histogram, obtaining the spatial distribution of the nuclei when they cross through the focal plane. This plot can be seen in Figure 4.2.
In each one of the ten sections the signals of the two central wires have been summed up creating a sharped peak just in the middle of each 10-cm-segment, these peaks are used as reference points for the spatial calibration. It always must be checked that the full focal

plane histogram do not present discontinuities in the count rate betweeen adjacent sections, a discontinuity of the counting intensity would mean a detection inneficiency in one of them, reducing the statistics available to be analysed [15]. An example of this problem is shown in figure 4.3

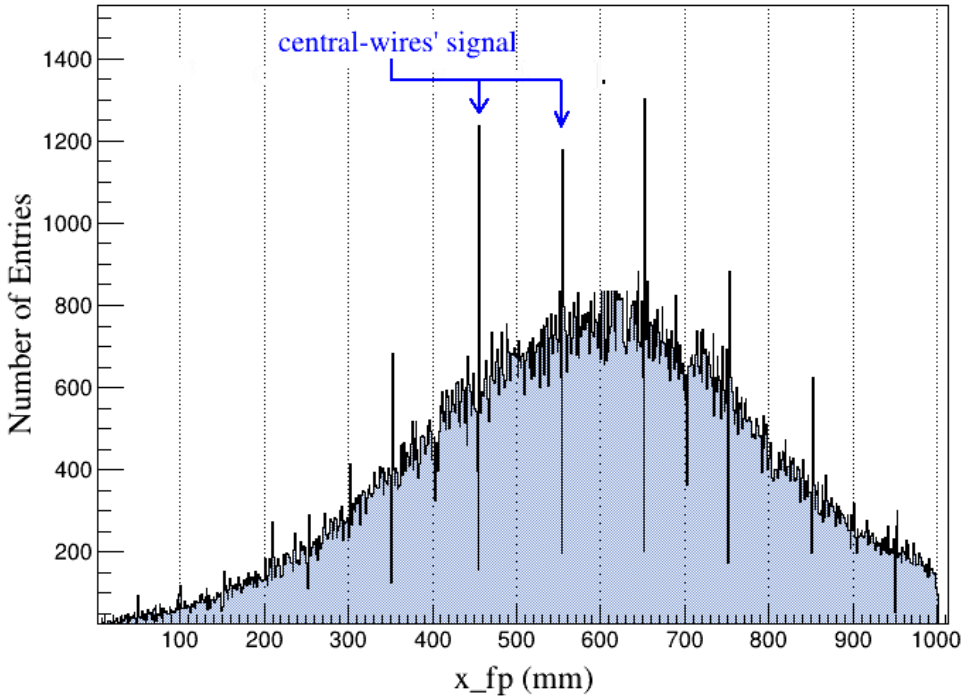

Figure 4.2: Alligned and calibrated X_fp events of the 10 MWPPAC sections.

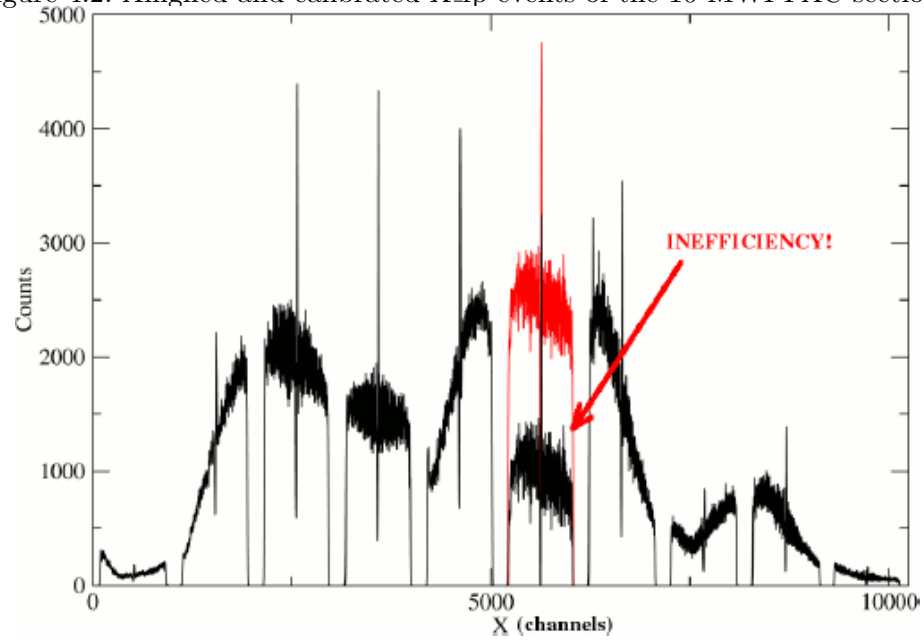

Figure 4.3: **Top** Typical MWPPAC histogram, it shows the horizontal position distribution for the incoming ions that reached PRISMA. **Bottom** Example of MWPPAC histogram with inefficiency in the fifth section. In red, the spectrum as it should look like, taken from [15].

4.1.3. TOF Calibration

The Time-Of-Flight is computed as the time difference between the stop and start signals. Each one of the MWPPAC sections provide an independent stop time signals, and therefore independent TOF measurement that must be calibrated in time units. The TOF vs. X_fp plot is shown in Figure 4.4. The horizontal line at the top of each 10 cm-spectrum corresponds to events with a missing time signal for which a default TOF value has been assigned. These events are excluded from the analysis and only nuclei with TOF$\leq$335 ns are regarded, the corresponding plot can be seen in Figure 4.4.

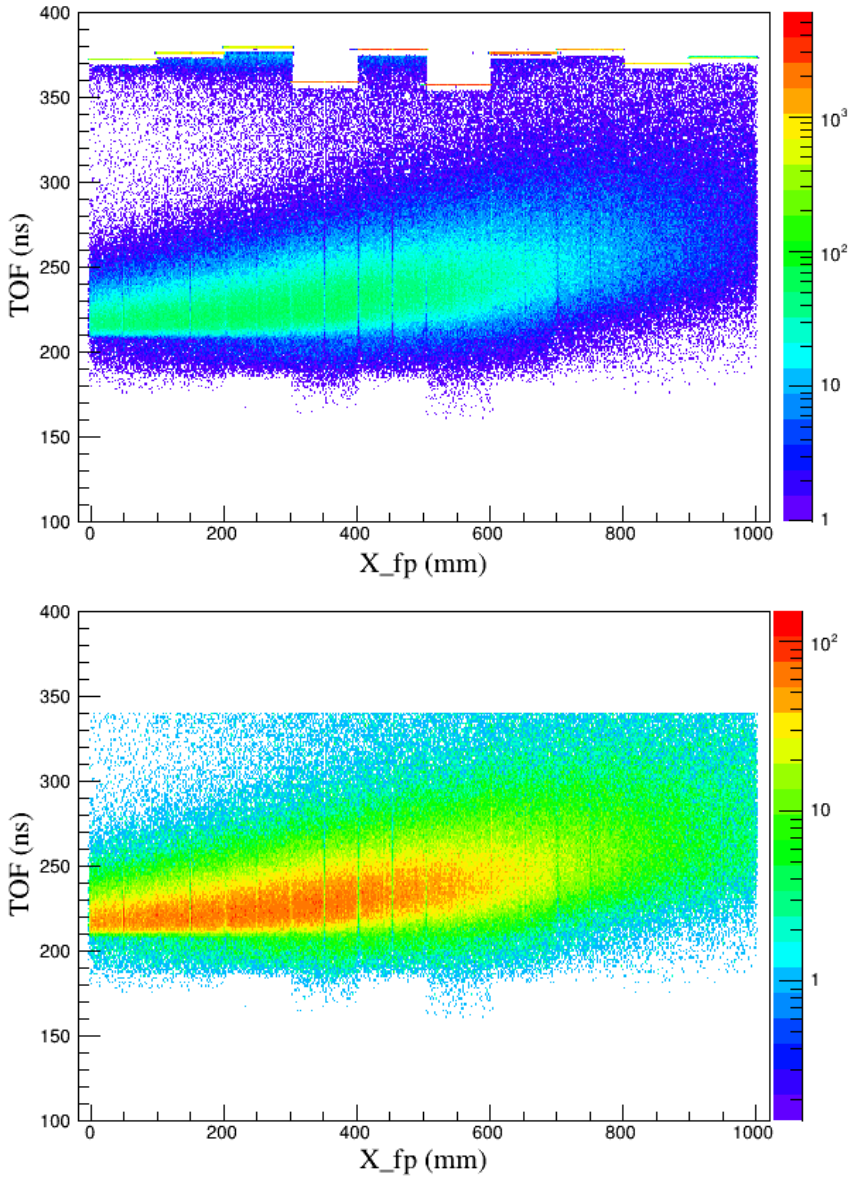

Figure 4.4: **Top.** calibrated TOF vs. X_fp plot, including the default TOF signals. **Bottom.** TOF vs. X_fp plot of events with TOF$\leq$340 ns.

4.2. Atomic number (Z) identification

The mean rate of energy loss of a heavy charged particle when it crosses a dense material, just as in the case of a detected nucleus traversing the ionization chamber filling gas in PRISMA, is given by the Bethe-Bloch formula

$$\frac{dE}{dx} = \frac{Z^2}{(\beta c)^2}\left[\frac{\rho z N_0 e^2}{Am\epsilon_0}\right]\left[\ln\left(\frac{2mc^2\beta^2}{I(1-\beta^2)}\right) - \beta^2\right], \tag{4.1}$$

where Z and $v = \beta c$ stand for the nucleus atomic number and velocity. ρ, z, and A, represent the density, atomic number, and mass of the stopping material, respectively. N_0 stands for the Avogadro's number, m and e the electron's mass and charge, and I the mean excitation energy of the stopping material [14]. In the non-relativistic regime it is valid that $v^2 = 2E/M$, and equation (4.1) is commonly aproximated to

$$\frac{dE}{dx} \propto \frac{MZ^2}{E} \quad \Rightarrow \quad \Delta E \propto \frac{MZ^2}{E}\Delta x. \tag{4.2}$$

This equation expresses that the amount of energy ΔE lost by the nucleus after traversing a distance Δx through the stopping material is proportional to the ratio MZ^2/E. Therefore, two particles with different Z can be distinguished by measuring and comparing their energy loss ΔE when they cross through a same material.
A segmented particle detector is composed by an array of adjacent but independent sections designed for a nucleus to lose only a fraction of its energy in each section but being completely stopped before it crosses the full array. This design allows the measurement of ΔE as well as the total energy E, see Figure 4.5.

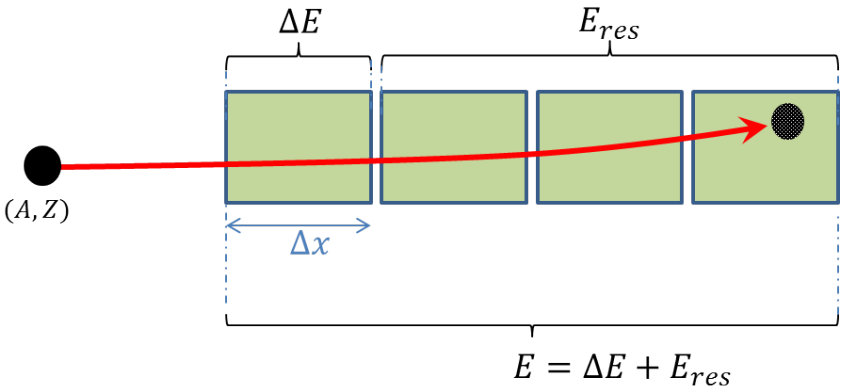

Figure 4.5: ΔE-E detector scheme.

For the experiment under study, ΔE corresponds to the energy loss in the first two segments of the IC array. This election was done since it was noticed that this criteria allowed a more clear identification of Z than considering ΔE as the energy loss only in the first segment. The ΔE vs. E histogram plot is shown in Figure 4.6. For $\Delta E > E$ there are no counts since it is not possible for the energy loss in a fraction of the detector to be higher than the total

energy released on it. Some of the nuclei were almost or completely stopped in the first two segments of the IC array, these correspond to the high number of counts near the $\Delta E = E$ line . For $\Delta E < E$ it can be distinguished several tilted lines, each one is a region composed of events with the same atomic number Z. The one with the highest statistics corresponds to the beam isotopes of Xenon ($Z_{Xe} = 54$) scattered at the reaction's grazing angle. This happens because the Coulomb excitation interaction has the highest cross-section process of the experiment [15], as it was explained in section 2.1.

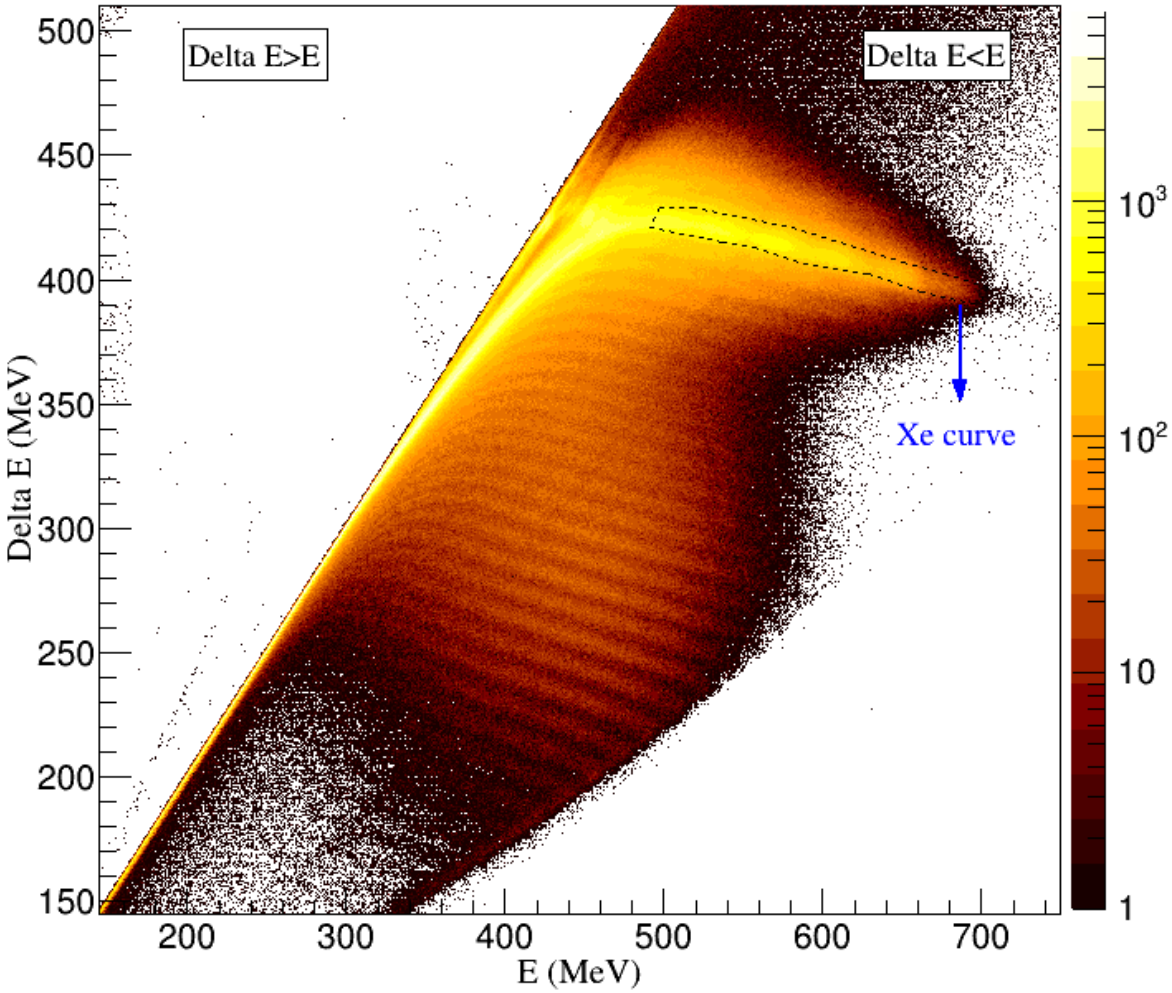

Figure 4.6: ΔE vs E plot. Notice the curved-line regions for $\Delta E¡E$, each one corresponds to a different family of isotopes populated in the reaction.

The assignment of Z is very straightforward using the Xenon *line* as a reference: For a constant energy E it happens that the value of ΔE decreases with Z, therefore, the first line below corresponds to Iodine ($Z_I = 53$), the second one to Tellurium ($Z_{Te} = 52$), and so on. Events with the same Z number are grouped using a **Graphical Cut**, a hand-made

polygon enclosing the plot region where the events of interest are located. The set of cuts enclosing all the different elements detected in the experiment are shown in Figure 4.7.

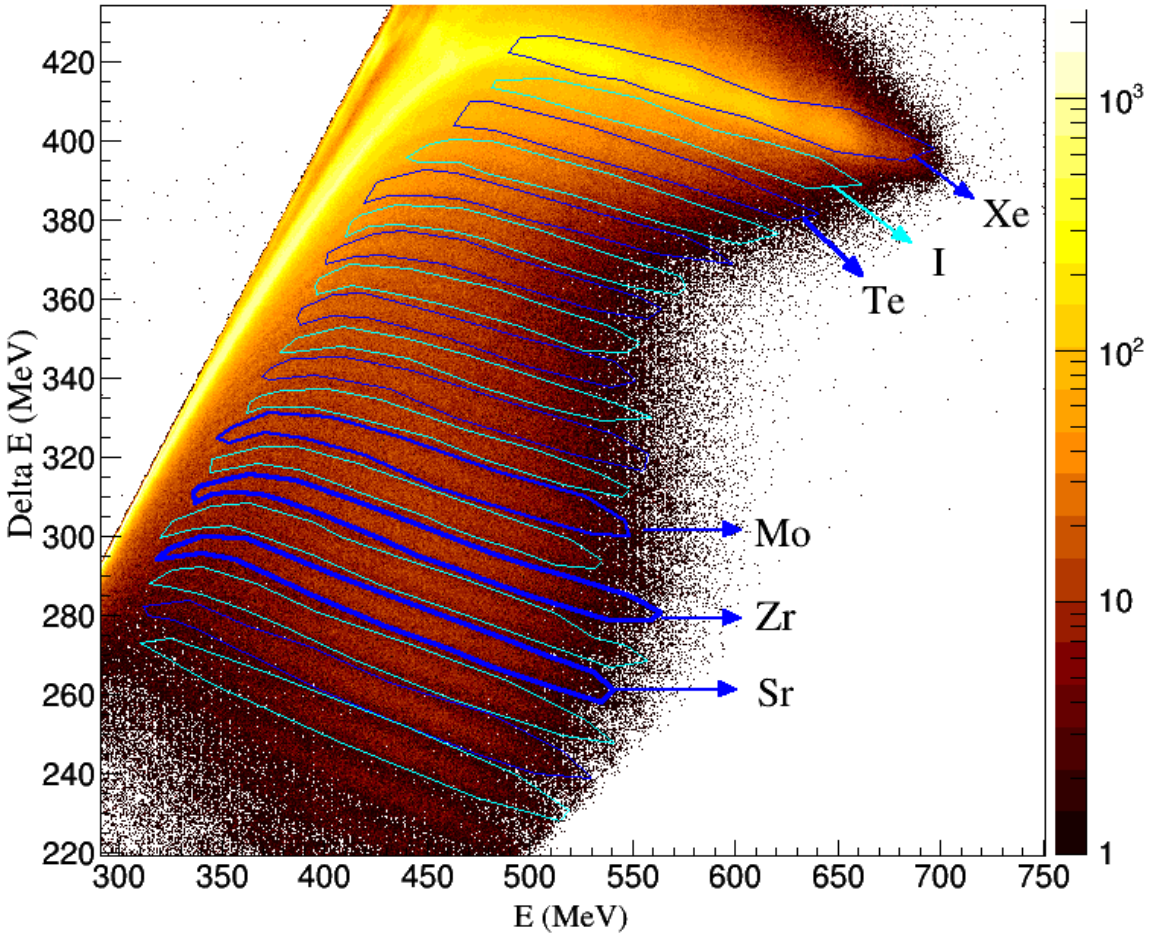

Figure 4.7: Graphical cuts enclosing events with common Z.

4.3. Mass number identification

For the mass number identification process only events with the same Z number are used. The nuclei to be analized in the following sections of this chapter correspond to the Molybdenum isotopes (Z_{Mo}=42) detected by PRISMA. They have been selected using the **Mo** graphical cut shown in Figure 4.7. First, these events are classified by groups of common charge state, Q. Then, the histogram of the A/Q value is obtained for each group. Since Z and Q are fixed, this histogram corresponds to the mass distribution of isotopes of the element Z. Using the γ-rays in coincidence it can be determined the identity of some peaks in the mass distribution spectrum, providing a reference point to calibrate the mass distribution in atomic mass units. This process is explained in detail following.

4.3.1. Charge state (Q) identification

The motion of the nuclei when they cross through the PRISMA's Magnetic Dipole is ruled by the Lorentz force,

$$M\vec{a} = Q\vec{V} \times \vec{B_{dip}}. \tag{4.3}$$

Since the vertical component of the velocity is very low after the nuclei cross the magnetic quadrupole, it is assumed that $\vec{V}$ lies in the horizontal plane, perpendicular to $\vec{B_{dip}}$ [14]. The cross product between these quantities shows that the magnetic force is perpendicular to the velocity and constrains the nuclei to move in a circular trajectory, therefore, $|\vec{a}| = V^2/R$. The equation (4.3) can be re-expressed as,

$$\frac{MV^2}{R} = QVB. \tag{4.4}$$

Since $E = MV^2/2$, and $V = D/\mathrm{TOF}$, equation (4.4) can be re-expressed as

$$\frac{2E}{R} = QB\left(\frac{D}{TOF}\right) \tag{4.5}$$

$$E = Q \cdot \frac{B}{2} \cdot \left(\frac{RD}{\mathrm{TOF}}\right). \tag{4.6}$$

When the E vs. RD/TOF histogram of Molybdenum events is plotted (see Figure 4.8) they appear gathered in regions with straight-line shapes, each one has an slope proportional to the charge state Q of the events that it contains, in correspondence with Equation (4.6). Six different charge states were identified, the graphical cuts performed on each one of them are shown in Figure 4.8.

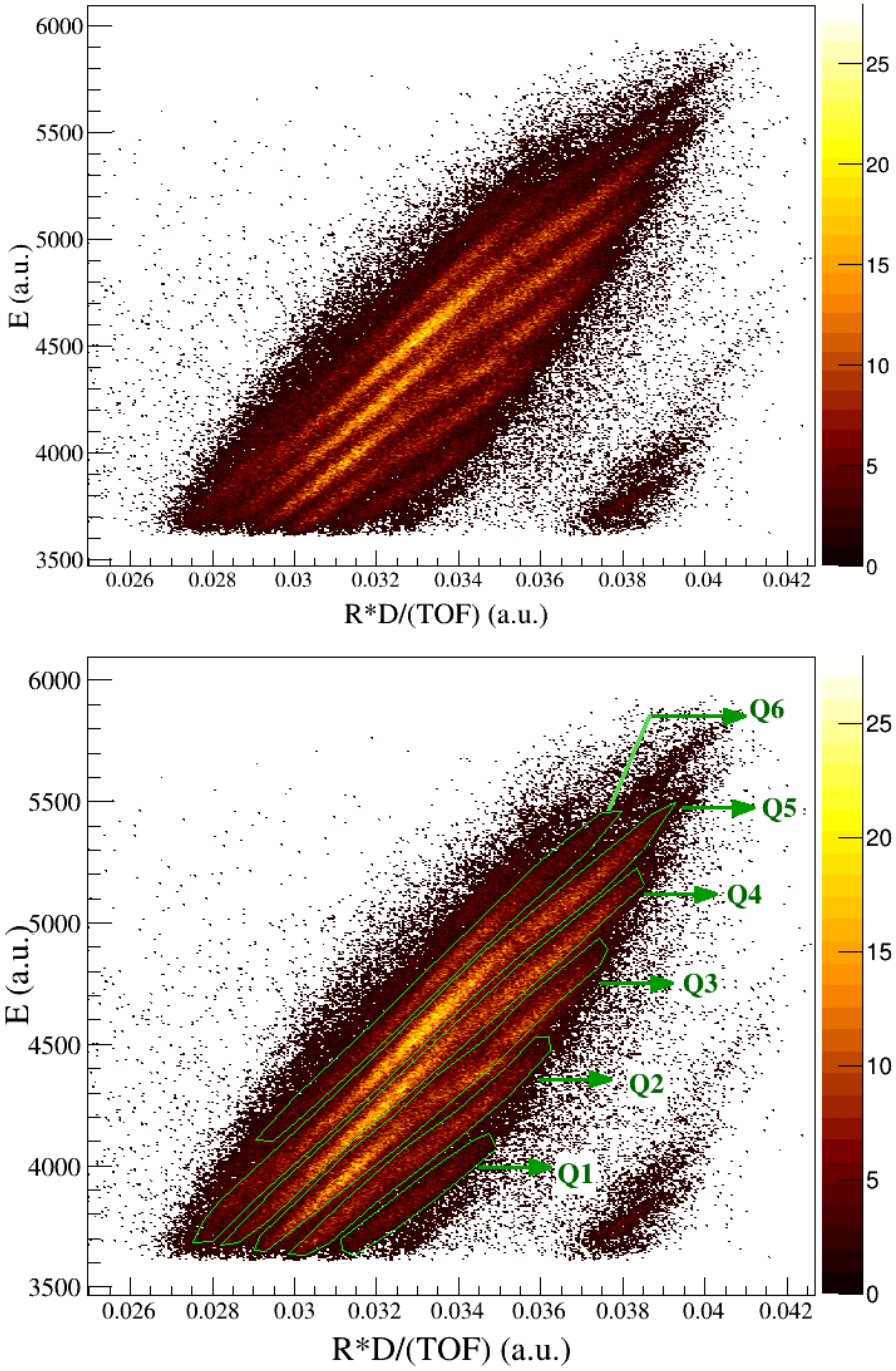

Figure 4.8: **Top**. E vs. $R{\cdot}V$ plot for Mo events. Each one of the visible *lines* is composed by isotopes with common Q. **Bottom.** Cuts created in order to group events by Q.

4.3.2. A/Q histograms

Once a set of Mo isotopes with common Q is chosed using one of the graphical cuts created in Figure 4.8, their mass number A can be obtained straightforward. Using the Lorentz force equation,

$$\frac{MV^2}{R} = QVB \tag{4.7}$$

$$\frac{M}{Q} = \frac{RB}{V}. \tag{4.8}$$

Since the mass M is proportional to the mass number A, equation (4.8) leads to,

$$\frac{A}{Q} \propto \frac{M}{Q} = \frac{RB}{D/\mathrm{TOF}} \tag{4.9}$$

$$\frac{A}{Q} \propto \frac{R \cdot \mathrm{TOF}}{D}. \tag{4.10}$$

The A/Q value is obtained event by event using equation (4.10) in order to obtain an A/Q histogram for the particular Q choosed previously. The A/Q histograms for the set of events with Q4, Q5, and Q6, are shown in Figure 4.9. Each one shows equidistant peaks that correspond to the masses of the different Mo isotopes detected during the experiment. For the charge states Q1, Q2, and Q3, the A/Q histograms are not shown since they don't have enough statistics and no peaks clearly defined can be recognized.

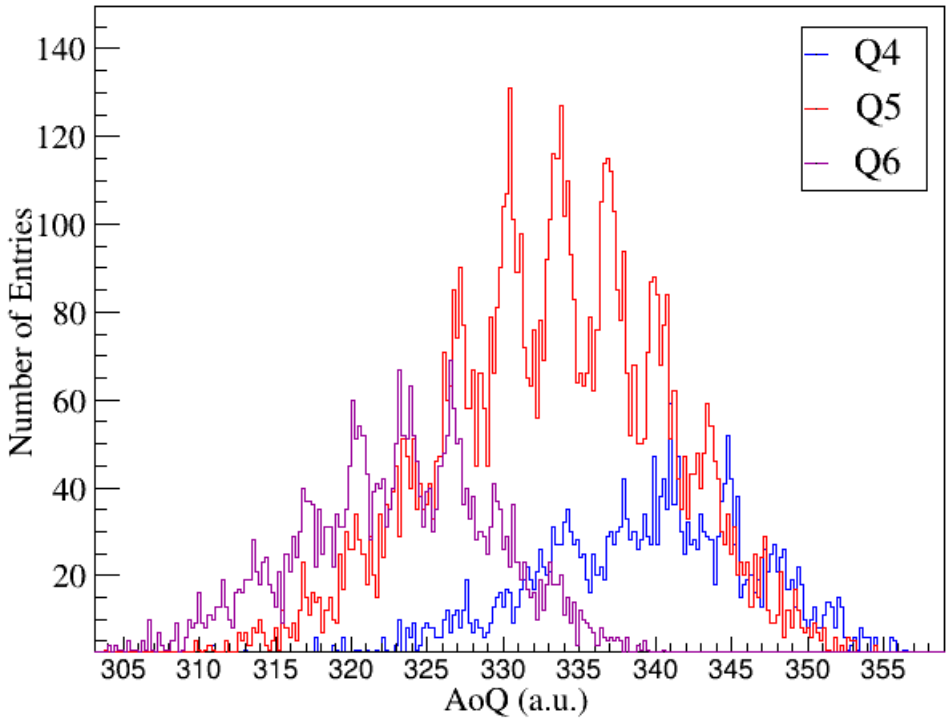

Figure 4.9: A/Q histograms for the Molybdenum events grouped by charge state.

4.3.3. Mass Calibration

In order to know which specific Mo isotope corresponds to each peak in a particular A/Q histogram, the energy spectrum of the γ-rays in coincidence with the events in at least one peak must be checked. The energies of the photo-peaks found in the spectrum are compared with the energies of the reported transitions of the several neutron-rich Molybdenum isotopes currently known, specifically with the low-excitation energy transitions, which are the ones of intereset in this work. Once the identity of one of the peaks has been assigned, the matching process is repeated for the nearby peaks to guarantee that the assignment previously done is univoque, this process is shown in Figure 4.10. For the charge state Q5, the γ-rays in coincidence with the peaks a, b, and c, reveal the main transitions of ^{102}Mo, ^{104}Mo, and ^{106}Mo, respectively. The corresponding level schemes of these nuclei can be found in Appendix A.

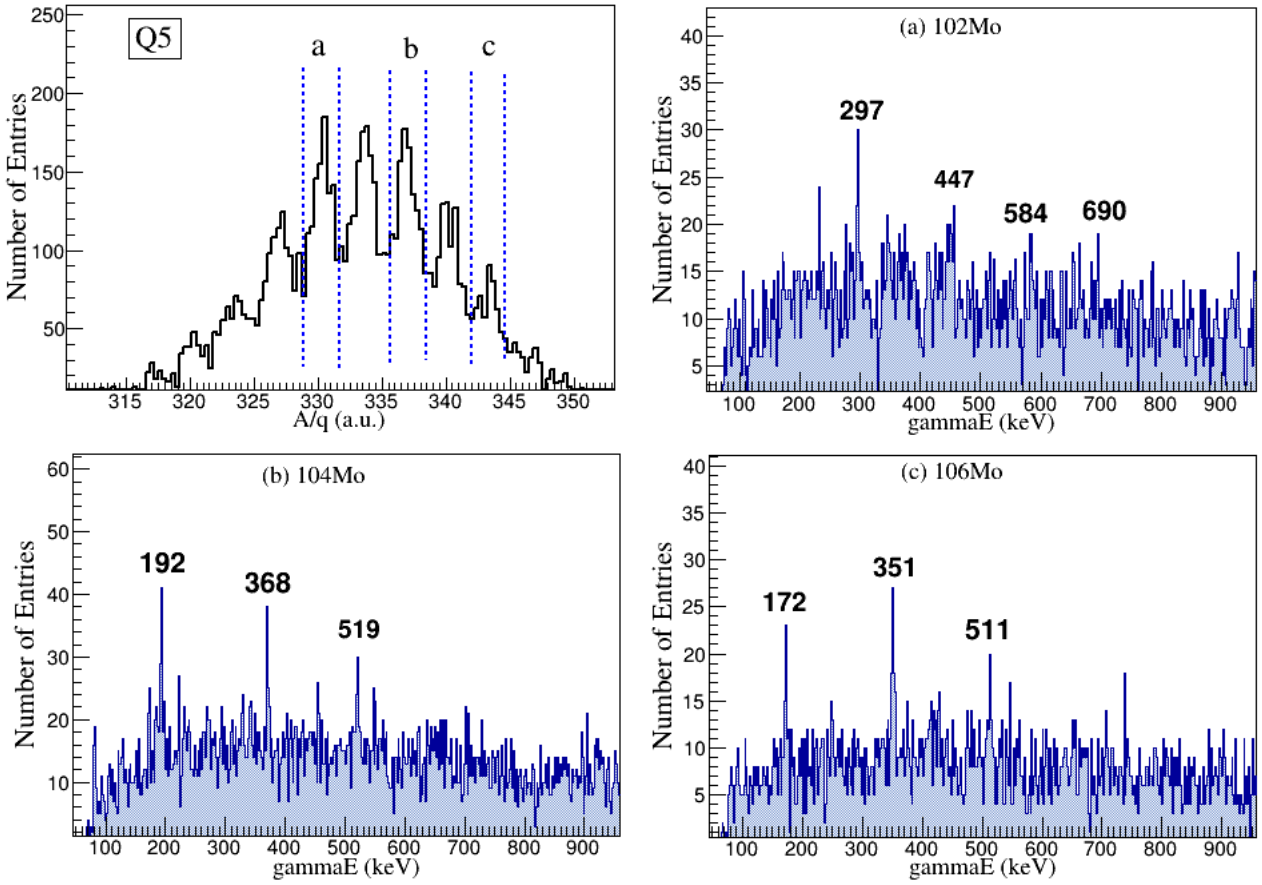

Figure 4.10: **Top-Left.** A/Q histogram for Q5; the peaks that correspond to the isotopes ^{102}Mo, ^{104}Mo, and ^{106}Mo, are labeled as a,b, and c, respectively. The energy spectrum of the γ-rays in coincidence with the events in these peaks are shown in the subplots (a), (b), and (c).

The A/Q histogram range must be calibrated in mass units such that each peak will be located at the adequate integer mass number. Since the A/Q peaks are partially mixed then

the calibration is not simply to assign the integer mass values to the A/Q positions with the highest count in each peak. In order to find the *gaussian mean* of each peak, a multigaussian function

$$F(x) = \sum_{i=1}^{n} A_i \cdot \exp\left(-\frac{1}{2}\left[\frac{x - c_i}{\sigma_i}\right]^2\right),$$

with n the number of visible peaks, is fitted to the histogram, as it is shown in Figure 4.12. The A/Q positions obtained for the optimal gaussian means provide the most adecuate mass peak center, therefore, they are assigned to integer values of atomic mass units, as shown in Table 4.1.

optimal A/Q pos. (a.u.)	Mass (u.m.a)	optimal A/Q pos. (a.u.)	Mass (u.m.a)
320.07± 0.09	99.0	336.99± 0.05	104.0
323.52± 0.17	100.0	340.18± 0.10	105.0
327.05± 0.08	101.0	343.52± 0.11	106.0
330.40± 0.06	102.0	346.54± 0.27	107.0
333.68± 0.06	103.0		

Table 4.1: Optimal Gaussian means and their corresponding atomic mass value.

The A/Q positions are transformed in mass units via a linear function A=m·(A/Q)+b. The parameters used are found through the linear fitting of the values in Table 4.1, as it is shown in Figure 4.11. The optimal parameters found are $m = 0.3027(4)$ a.m.u, and $b = 2.0(3)$ a.m.u.

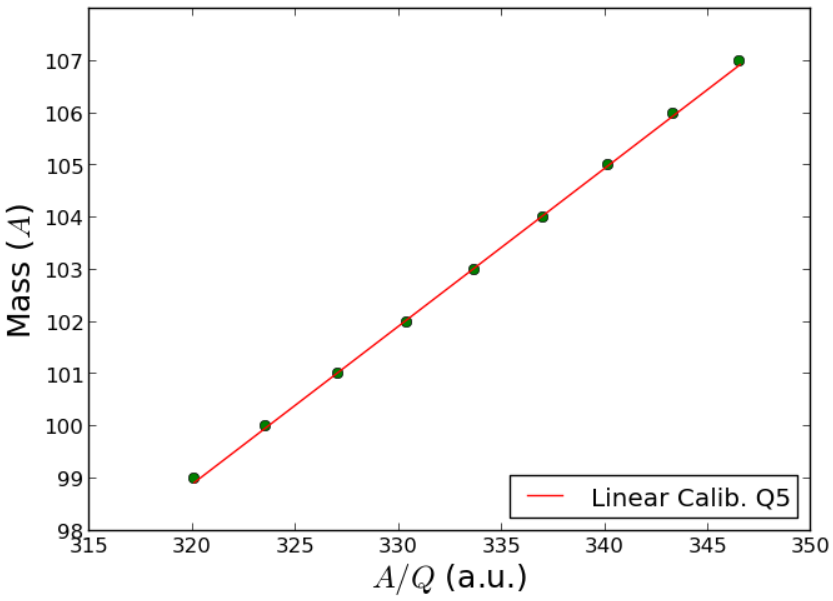

Figure 4.11: Linear fit of data in Table 4.1.

The mass calibration of Mo isotopes completed is shown in Figure 4.12, it shows the multi-gaussian fit for the A/Q histogram, and the corresponding calibrated mass spectrum.

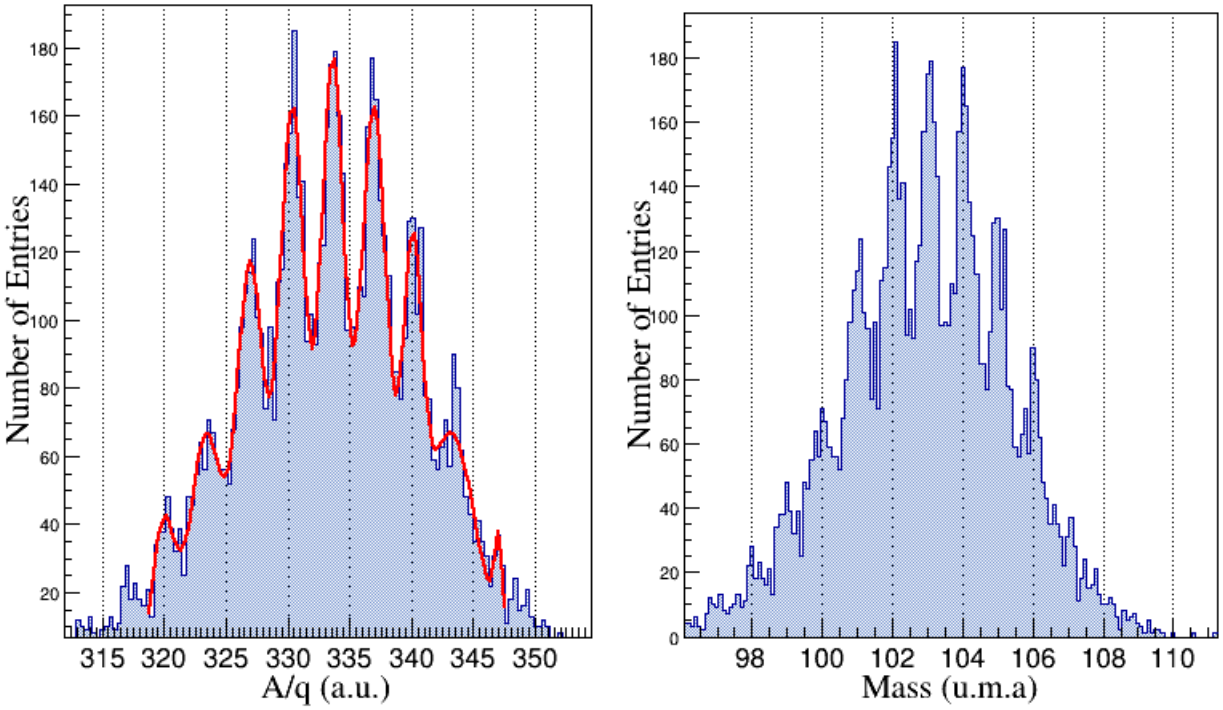

Figure 4.12: **Left** MultiGaussian fit performed on the A/Q histogram. **Right** Mass histogram obtained.

The mass resolution is defined as the width of the mass peaks at the half of their maximum height; this parameter is an indication of the PRISMA's performance to distinguish nearby nuclei. The mass resolution obtained for the Molybdenum spectrum is $\Delta m = 0.38 \pm 0.06$ u.m.a.

5 Results & Conclusions

In this chapter the distribution of the different chemical elements produced during the experiment and detected at the grazing angle, θ_g, is shown. Then, the mass distribution obtained for the Zr and Sr events is analysed together with the energy spectrum of the γ-rays in coincidence. Some conclusions and comments for this work are presented.

5.1. Distribution of Z

In order to quantify the *yield of production* of the different families of isotopes populated and scattered at the grazing angle direction, the number of detected events for each Z produced is computed as it is shown in Table 5.1. The obtained distribution can be seen in Figure 5.1. It shows the large number of nuclear species in which the ^{136}Xe beam nuclei were fragmented after colliding against the ^{238}U target. Notice that even at the θ_g direction, where DIC channels present their highest scattering cross section, the number of events corresponding to Coulomb excitation or neutron transfer channel -i.e. the Xe bar in the figure- is still much larger than any other.

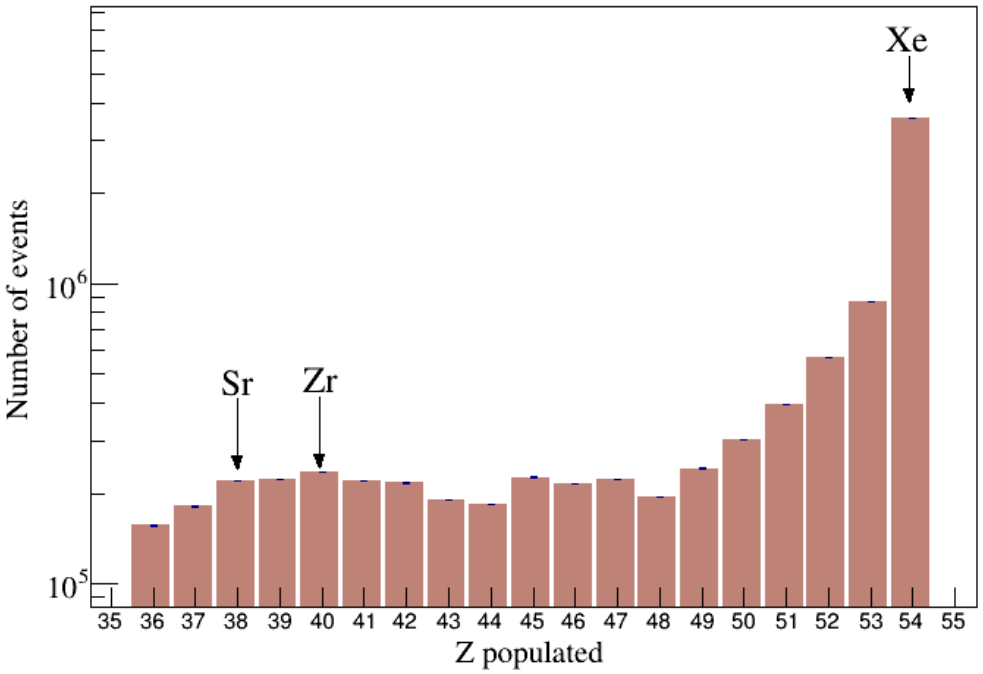

Figure 5.1: Z distribution detected by PRISMA in the θ_g direction.

Z	Isotope	Number of events	Z	Isotope	Number of events
54	Xe	$(3550.3\pm 1.8)\cdot 10^3$	44	Ru	$(184.1 \pm 0.4)\cdot 10^3$
53	I	$(870.1 \pm 0.9)\cdot 10^3$	43	Tc	$(190.4 \pm 0.4)\cdot 10^3$
52	Te	$(566.2 \pm 0.7)\cdot 10^3$	42	Mo	$(216.9 \pm 0.4)\cdot 10^3$
51	Sb	$(395.1 \pm 0.6)\cdot 10^3$	41	Nb	$(220.5 \pm 0.4)\cdot 10^3$
50	Sn	$(301.5 \pm 0.5)\cdot 10^3$	40	Zr	$(235.6 \pm 0.5)\cdot 10^3$
49	In	$(242.4 \pm 0.4)\cdot 10^3$	39	Y	$(222.7 \pm 0.4)\cdot 10^3$
48	Cd	$(194.1 \pm 0.4)\cdot 10^3$	38	Sr	$(220.8 \pm 0.5)\cdot 10^3$
47	Ag	$(222.2 \pm 0.4)\cdot 10^3$	37	Rb	$(181.1 \pm 0.4)\cdot 10^3$
46	Pd	$(215.1 \pm 0.4)\cdot 10^3$	36	Kr	$(156.4 \pm 0.3)\cdot 10^3$
45	Rh	$(226.4 \pm 0.4)\cdot 10^3$	-	-	-

Table 5.1: Number of detected events of each Z populated in the experiment.

5.2. Zirconium case

The following events to be analysed were selected using the **Zr cut** shown in Figure 4.7.

5.2.1. Mass Calibration

Seven different charge-states of Zr were detected, however, not all of them registered enough γ-rays in coincidence in order to assign a mass to the A/Q peaks. The usable Zr charge-state cuts are shown in Figure 5.2, and their corresponding A/Q histograms in Figure 5.3.

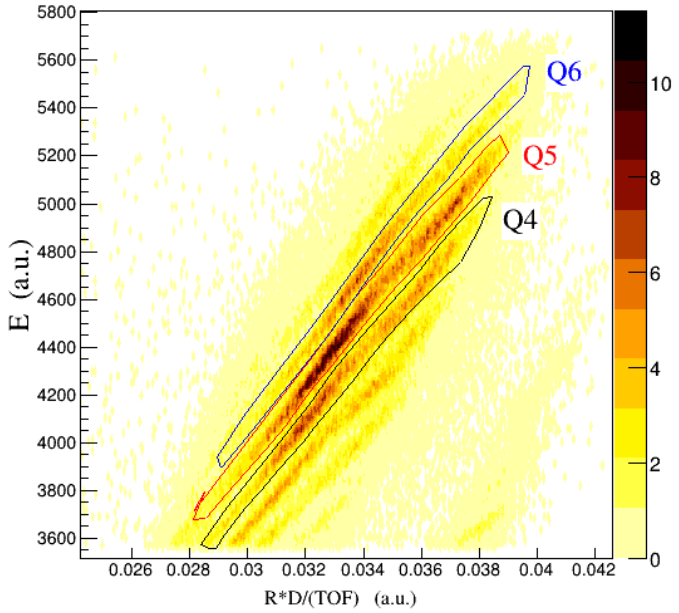

Figure 5.2: Charge-state cuts for Zr events.

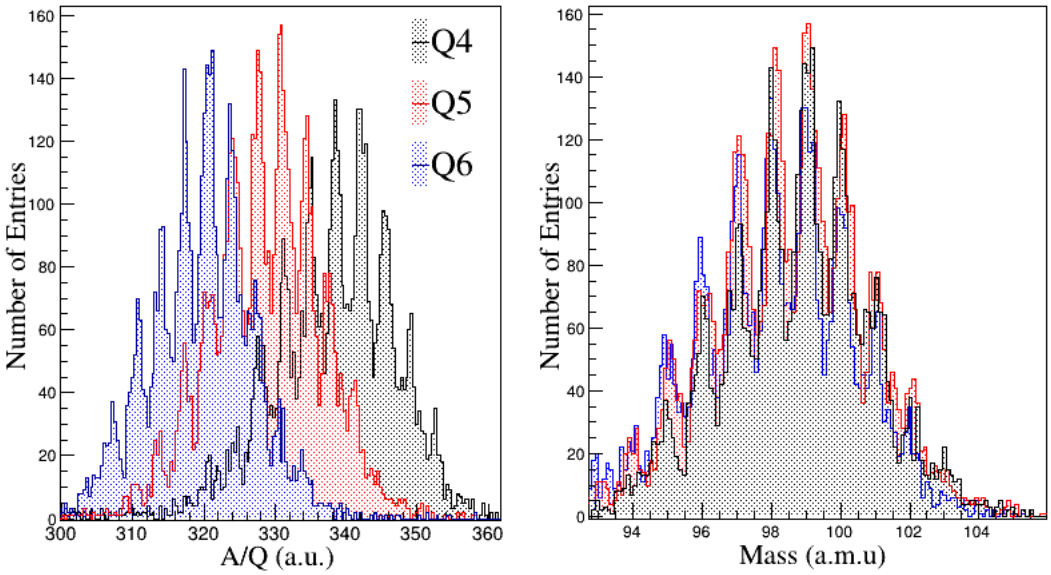

Figure 5.3: A/Q histograms for the events with the same charge states.

From Figure 5.3 it can be seen that the mass distribution is very similar for each charge state analysed, this happens because the neutrons transference process is only related with nuclear interactions, and not with atomic properties such as the charge state of the nucleus.

5.2.2. Mass Distribution

The total mass distribution obtained for the Zirconium detected events is shown in Figure 5.4. From the set of isotopes that were expected to study in this work, it was possible to populate ^{100}Zr, ^{102}Zr, and ^{104}Zr. For the first two nuclei a strong production was obtained, however, a very low number of events were detected for the last one, see Figure 5.4. The mass resolution associated to the Zr isotopes is in average $\Delta m = 0.37 \pm 0.08$ u.m.a. Nevertheless, it must be pointed out that the mass resolution as a function of the isotopic mass does not remain constant since for the low populated nuclei (A<93 or A>103) there is not statistics enough to define clear mass peaks.

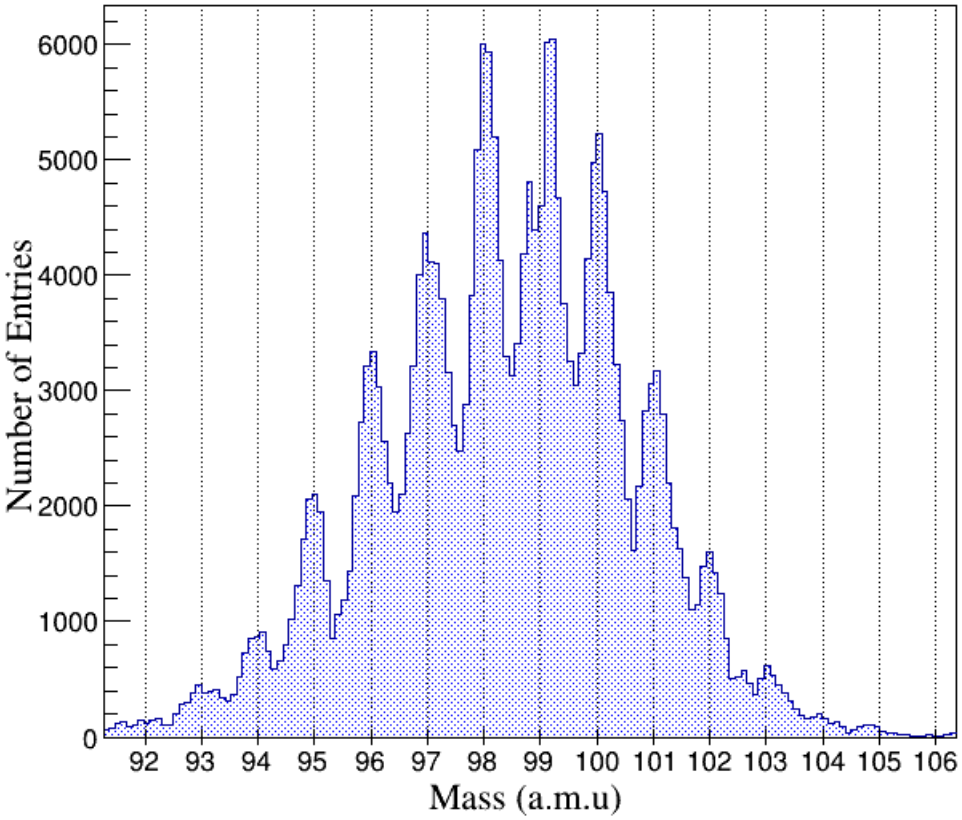

Figure 5.4: Mass distribution of Zirconium isotopes populated during the experiment.

5.2.3. Energy spectra of γ-rays in coincidence

The energy spectra of the γ-rays detected in coincidence with the isotopes ^{100}Zr, ^{102}Zr, and ^{104}Zr are shown below. It was found that the main peaks in these spectra correspond to the low excitation energy transitions that reproduce a fraction of the level scheme decay known for these isotopes shown in Appendix A, they can be consulted also in Ref. [1]. Figure 5.5 shows the peaks corresponding to the transitions of ^{100}Zr labelled with the energy position of the peak center. The high-energy peaks correspond to de-excitation from high-excitation energy states, populating these states is less probable than populating only the first excited state, this fact, combined with the decreasing efficiency of γ-ray detectors for higher energies, is reflected in a low peak intensity for high excited levels.

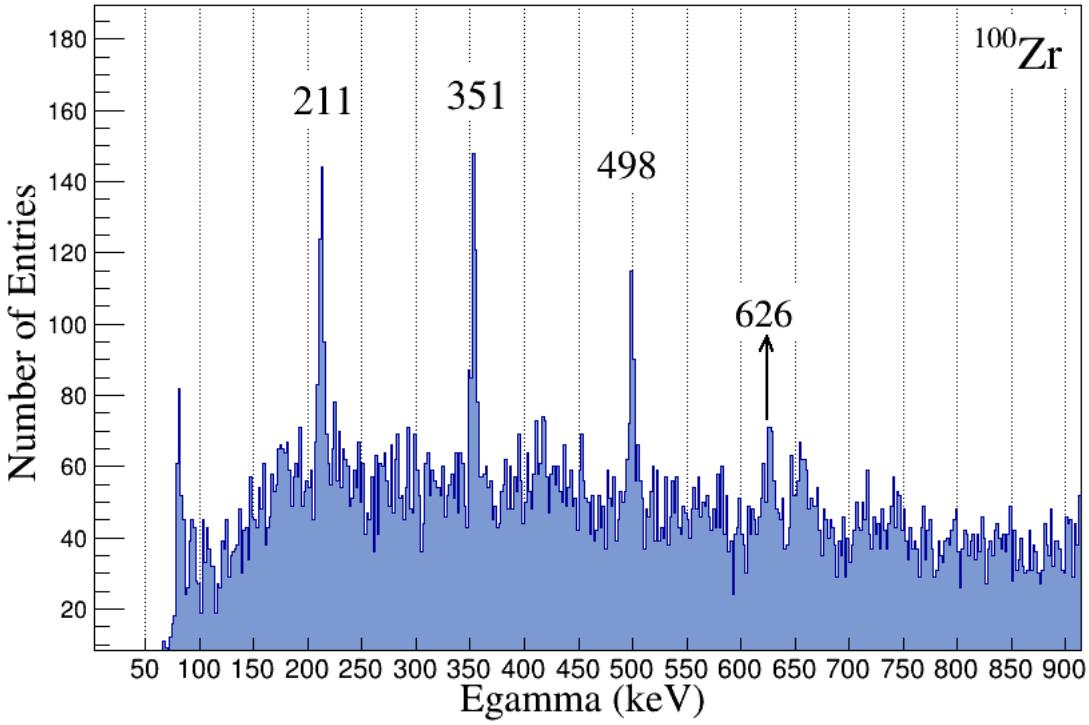

Figure 5.5: Energy spectrum of γ-rays in coincidence with ^{100}Zr. The visible peaks correspond to transitions of low excitation energy states (see the level scheme at Figure A.2.).

Figure 5.6 shows lowest-energy transitions of ^{102}Zr. The peak located at 405 keV does not correspond to any known transition for ^{102}Zr, it can be candidate to be a new transition for this nucleus since the gates imposed on the events registered in this spectrum guarantee that all the photons detected with this energy are in temporal coincidence with Zirconium nuclei with a computed mass of $102.0\pm\Delta m$. For this range in the mass spectrum there is an small overlap of events from ^{101,103}Zr not big enough to generate this peak. However, its number of counts (36 ± 6) is not large enough with respect to the background counts (25 ± 5) to claim that this peak is not a random background statistical effect. It was not possible to check if this peak is in coincidence with some of the observed transitions for ^{102}Zr because

the statistics available is not large enough to perform this procedure.

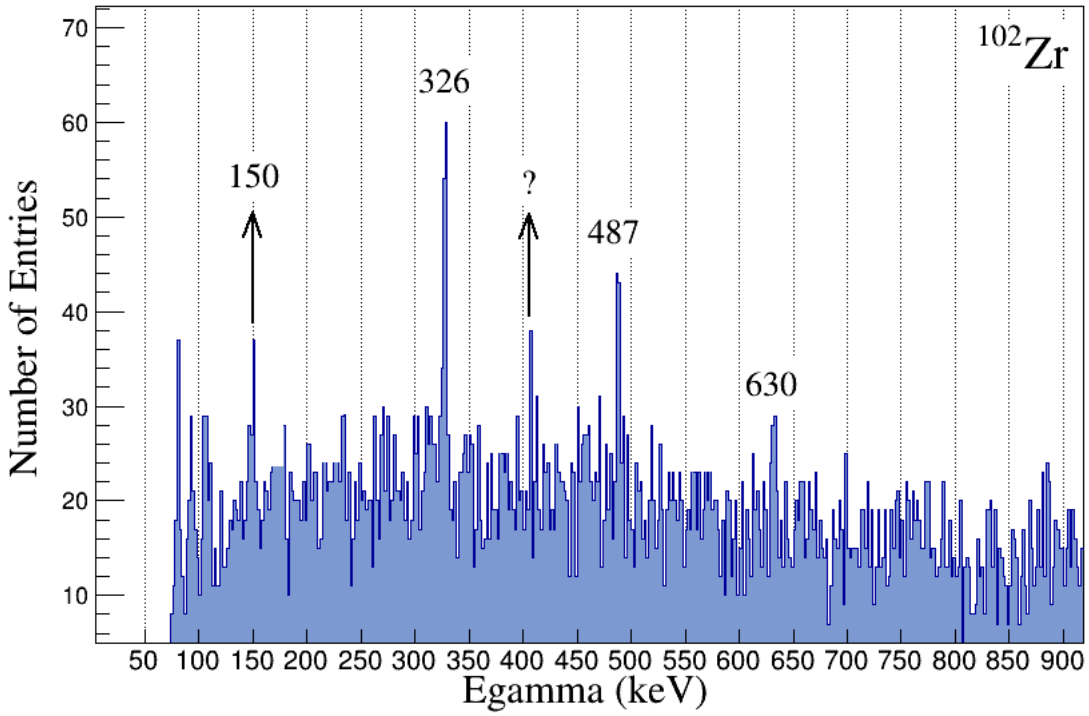

Figure 5.6: Energy spectrum of γ-rays in coincidence with ^{102}Zr. The transitions of the lowest excited states are visible. A peak at 405 keV can correspond to a new transition.

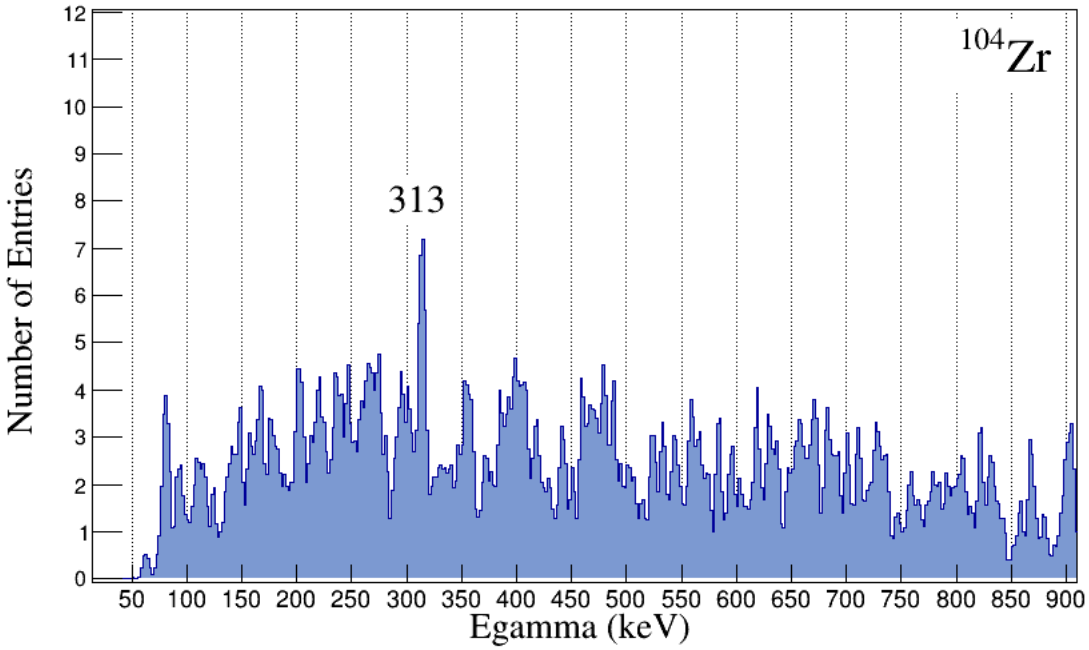

Figure 5.7: Energy spectrum of γ-rays in coincidence with ^{104}Zr. Only the 4+→2+ transition was possible to be detected.

Figure 5.7 shows the energy spectrum of γ-rays in coincidence with ^{104}Zr. The statistics available is very poor since the production of ^{104}Zr was weak, as it is shown in Figure 5.4. The first excited state is not identified in the spectra because this is an isomeric state with a life time of 2.0 ns, and therefore the transition does not take place near the collision zone but during the path toward PRISMA. In principle, with higher statistics this transition should be identified, just as in the case of the 2+*rightarrow*0+ transition of ^{102}Zr. It was possible to identify the transition 4+$\rightarrow$2+ excited state, with a value of 312 keV.

5.3. Strontium case

The following events to be analysed were selected using the **Sr cut** shown in Figure 4.7.

5.3.1. Mass Calibration

Six different charge-states were detected for Sr, however, not all of them registered enough γ-rays in coincidence in order to assign a mass to the A/Q peaks. The usable Sr charge-state cuts are shown in Figure 5.8, and their corresponding A/Q histograms in Figure 5.9.

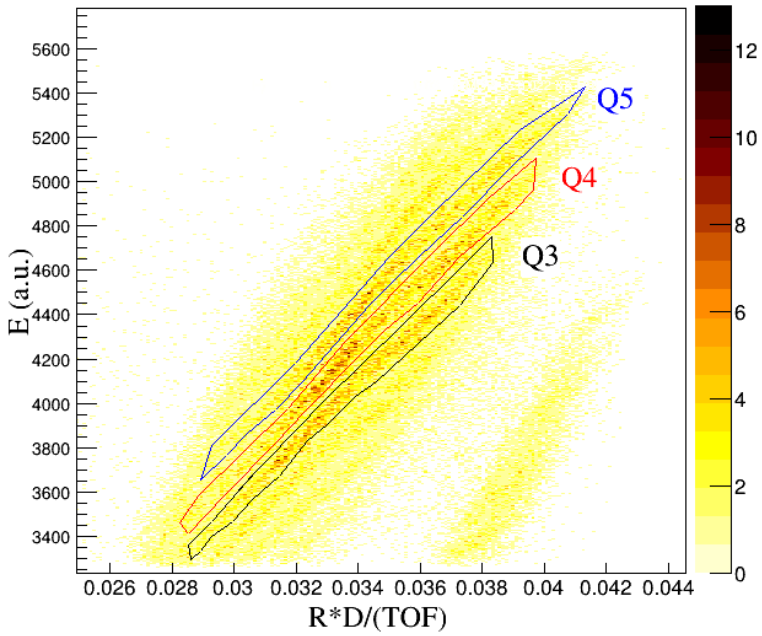

Figure 5.8: Charge-state cuts for Sr events.

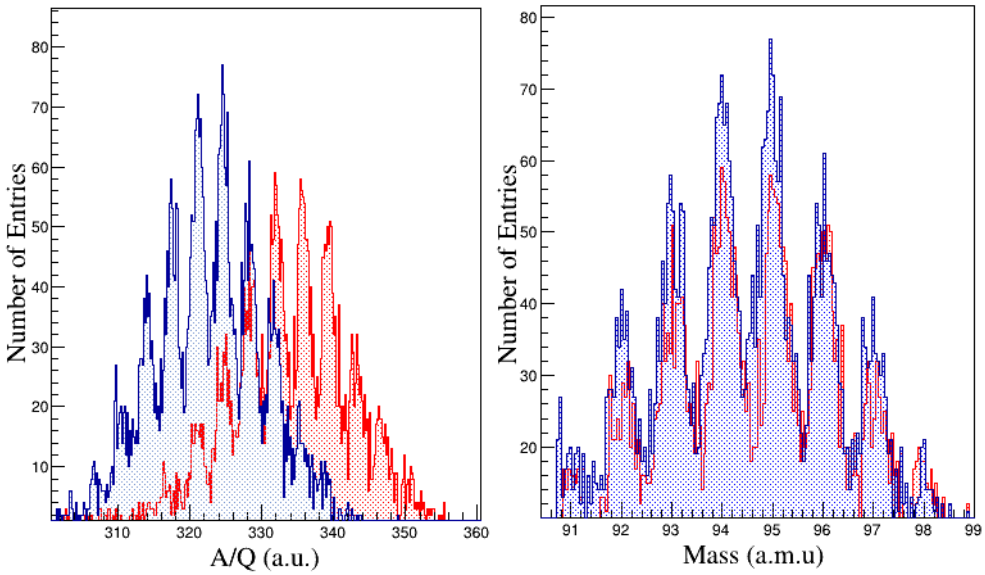

Figure 5.9: A/Q histograms for Sr events.

5.3.2. Mass Distribution

The total mass distribution obtained for the Strontium detected events is shown in Figure 5.10. From the set of isotopes that were expected to study in this work, it was possible to populate ^{100}Sr. However, a very low number of events were detected for this nuclei as it can be seen from the correspondent mass spectrum (see Figure 5.10). The mass resolution associated to the Sr isotopes is $\Delta m = 0.32 \pm 0.07$ u.m.a.

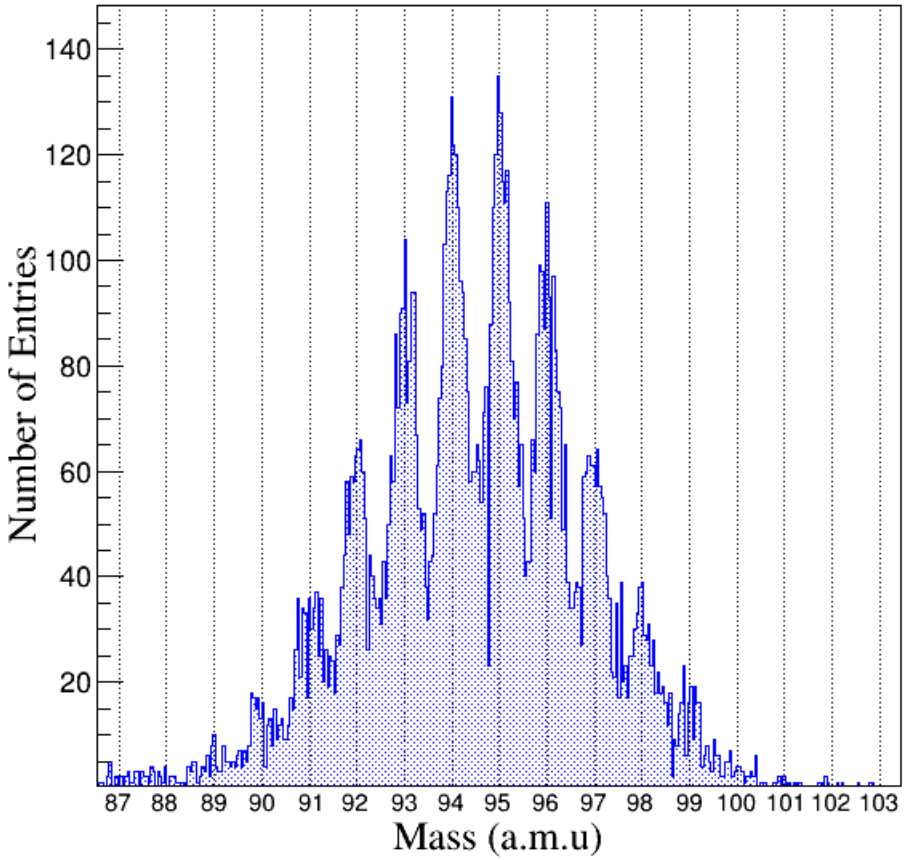

Figure 5.10: Mass distribution of Strontium isotopes detected by PRISMA.

5.3.3. Energy spectra of γ-rays in coincidence

Only for ^{96}Sr, and ^{98}Sr it was possible to produce energy spectra of the γ-rays detected in coincidence, these are shown below. Figure 5.11 shows to the two lowest-energy transitions of ^{96}Sr (compare with Figure A.3). This isotope present the largest background with respect to the all nuclei studied in this work. It can be seen different peaks that are not indicated with arrows since they do not correspond to ^{96}Sr or its closest neighbouring isotopes, and therefore their origin remain unknown.

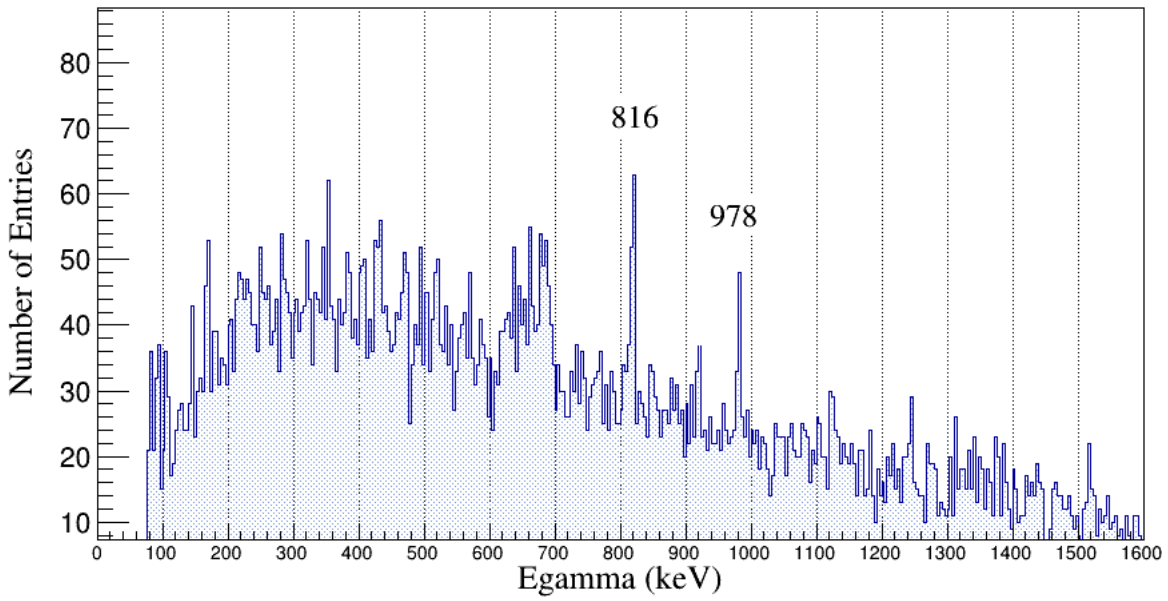

Figure 5.11: Energy spectrum of γ-rays in coincidence with ^{96}Sr.

Figure 5.12 shows the energy spectrum for ^{98}Sr. When the transitions registered are compare with the decay level scheme it can be seen that the transition of the first excited state is not present at all since it is an isomeric state with τ 2.8 ns.

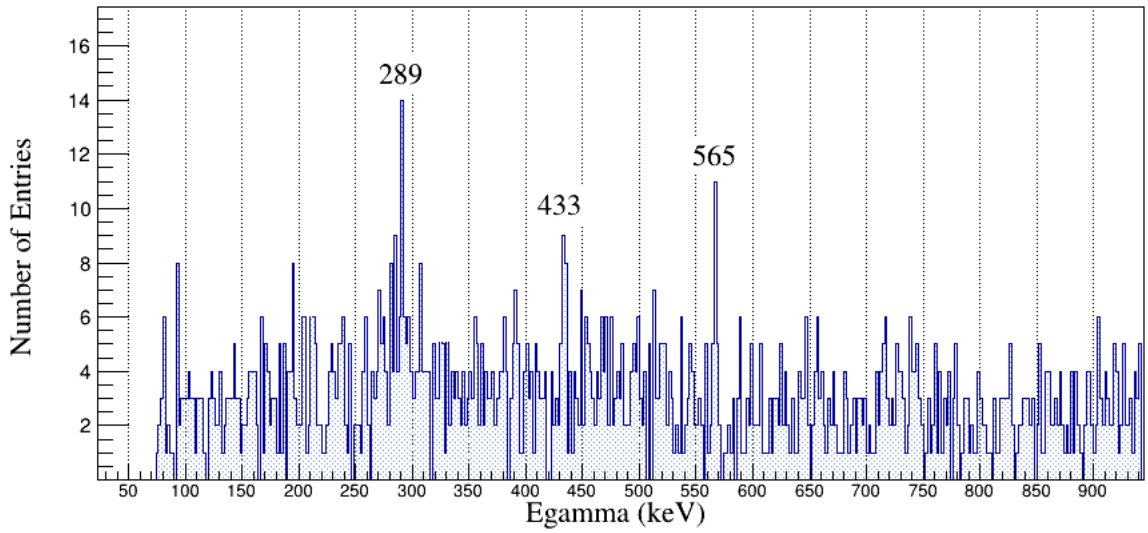

Figure 5.12: Energy spectrum of γ-rays in coincidence with ^{98}Sr.

5.4. Conclusions

- From the set of isotopes that were expected to study in this work, it was possible to populate ^{102}Zr, ^{104}Zr, and ^{98}Sr. For the first nucleus a strong production was obtained and four transitions were recognized. For the last ones, the transitions corresponding to the lowest excited states above the isomeric first excited states were possible to measure, a possible new transition of ^{102}Zr at 405 keV was observed, however, it is needed more statistics to investigate this hipothesis.

- Figure 5.7 shows the energy spectrum of γ-rays in coincidence with ^{104}Zr. The statistics available is very poor since the production of ^{104}Zr was weak, as it is shown in Figure 5.4. Nevertheless, It is possible to identify the transition of the $4+\rightarrow 2+$ transition, with a value of 312 keV.

- It can be seen that, even at the θ_g direction, where Deep Inelastic channels present the highest scattering cross section, the number of detected Xe events -i.e. Coulomb or neutron transfer channels- is larger by far.

A Decay level schemes

A decay level scheme is a visualization of the different energy levels for a particular isotope. Each level represented by a horizontal line is placed at a distance with respect to the bottom line -which corresponds to the ground state- proportional to the level excitation energy. They are usually labeled with the spin number (in $\hbar$ units), and the parity of the level (+,-). Each arrow joinning to levels correspond to a nuclear transition, the energy of the photon released is indicated next (keV energy units). In this appendix, the partial decay level schemes for the neutron-rich isotopes of Mo, Zr, and Sr, of interest are shown. A more complete level scheme for this nuclei can be found on Ref [1]. The red boxes indicates the transitions that were observed in the experiment performed.

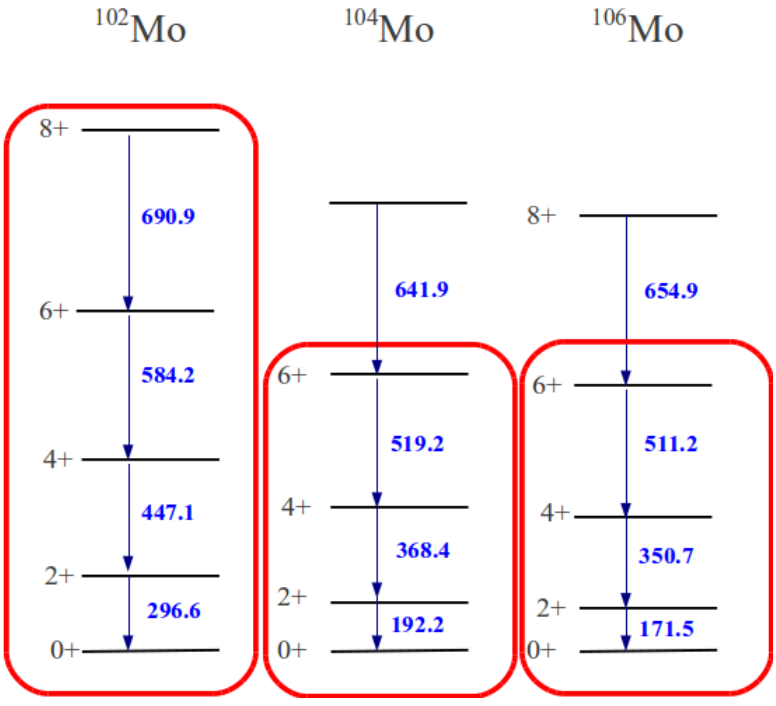

Figure A.1: Partial decay level schemes for even-even Mo Isotopes (Z=42).

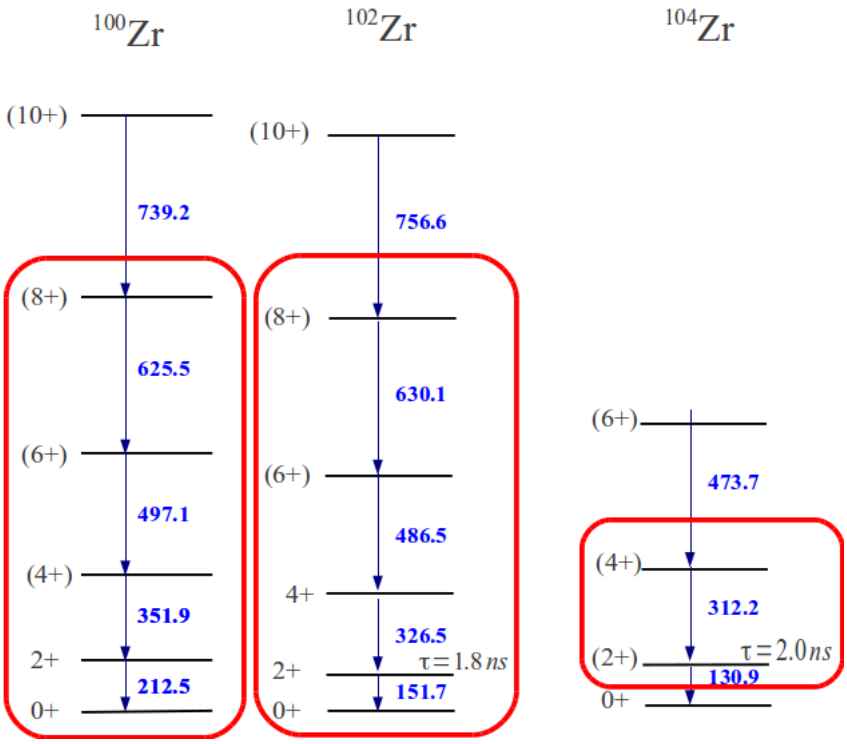

Figure A.2: Partial decay level schemes for even-even Zr Isotopes (Z=40).

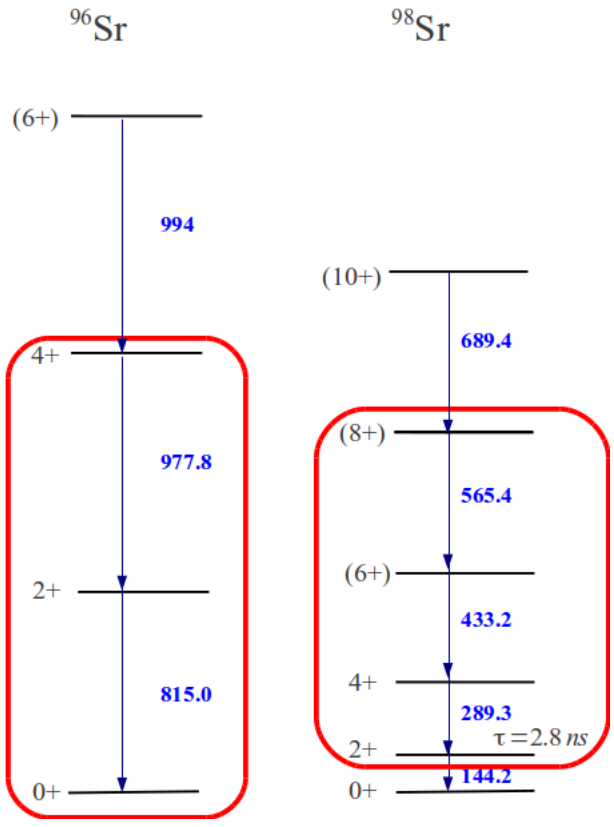

Figure A.3: Partial decay level schemes for even-even Sr Isotopes (Sr=38).

Bibliografía

[1] http://www.nndc.bnl.gov/chart/ - chart of nuclides.

[2] T. Sumikama. et al. Structural evolution in the neutron-rich nuclei 106zr and 108zr. *Phys. Rev. Lett*, 106, May 2011. 10.1103/PhysRevLett.106.202501.

[3] C.A. Ur et al, E. Merchán. *NRZ38 Experiment's proposal*, 2010.

[4] Fernando Cristancho. Estructura nuclear. Lecture Notes, October 2010.

[5] Walter Greiner. *Nuclear Models*. Springer, 2003.

[6] David Rowe. *Nuclear Collective Motion*. World Scientific, 2nd edition, 2008.

[7] Ben Mottelson Aage Bohr. Moments of inertia of rotating nuclei. In *Dan. Mat. Fys. Medd*, volume 30. Kobenhavn, 1955.

[8] R.B. Cakirli and R.F. Casten. Empirical signature for shape transitions mediated by sub-shell changes. *Phys. Rev. C*, 78(041301), 2008.

[9] F.R. Xu et al. *Phys. Rev. C.*, 65(021303), 2002.

[10] S. Mizutori J. Skalski and W. Nazarewicz. *Nucl. Phys. A*, 617:282, 1997.

[11] N. Schunk et al. *Phys. Rev. C*, 69(061305), 2004.

[12] Glendenning Norman K. *Direct Nuclear Reactions*. World Scientific, 2004.

[13] Gontchar I.I. Frobrich P. *Theory of Nuclear Reactions*. Oxford Science Publications, 1996.

[14] A. Gottardo. *Study of the neutron-rich nuclei with the CLARA-PRISMA setu and first test of the ancillary detector DANTE*. PhD thesis, Universita degli study dy Padova, 2007.

[15] A. Latina. *Study of Heavy-Ion Reactions with the Magnetic Spectrometer PRISMA: On-line and Off-line Data Analysis*. PhD thesis, Universita degli study dy Torino, 2007.

[16] Winther Aage. Grazing reactions in collisions between heavy nuclei. *Nuclear Physics*, A572:191–235, 1994.

[17] NÃ¶renberg Wolfgang. *Introduction to the Theory of Heavy-Ion Collisions*. Springer-Verlag, 1976.

[18] The large-area micro-channel plate entrance detector of the heavy-ion magnetic spectrometer prisma. *Nucl. Inst. and Meth. A*, 2005.

[19] E. Farnea on behalf of the AGATA Collaboration. http://cds.cern.ch/record/1537360/files/p387.pdf. Technical report, INFN Sezione di Padova, 35131 Padova, Italy, 2011.

[20] A. Latina E. Farnea. Monte carlo simulations of the agata demonstrator array coupled to the prisma magnetic spectrometer. Technical report, INFN Sezione di Padova, 2007.

[21] http://www-w2k.gsi.de/agata/overview.htm.

[22] Recchia Francesco. Installation of the agata demonstrator and commissioning experiments at lnl. *Journal of Physics: Conference Series 205*, 2010.

[23] et. al. Bart Bruyneel, Peter Reiter. Crosstalk properties of 36-fold segmented symmetric hexagonal hpge detectors. *Nuclear Instruments and Methods*, 599:196–208, 2009.

[24] http://www.lnl.infn.it/ prisma/it/index.html.

[25] G.Montagnoli et al. The large-area micro-channel plate entrance detector of the heavy-ion magnetic spectrometer prisma. *Nucl. Inst. and Meth. A*, 2005.

[26] A.M Stefanini et al. The heavy-ion magnetic spectrometer prisma. *Nucl. Inst. and Meth. A*, 2002.

[27] Nrz38 experiment's logbook, July 2011.

[28] http://root.cern.ch/drupal/.

[29] http://www.ipnl.in2p3.fr/gammaware/doc/html/.